

Banner appropriate to article type will appear here in typeset article

# Nonlinear evolution of vortical disturbances entrained in the entrance region of a circular pipe

Kaixin Zhu<sup>1</sup> and Pierre Ricco<sup>1</sup>†

<sup>1</sup>Department of Mechanical Engineering, The University of Sheffield, Sheffield, S1 3JD, UK

(Received xx; revised xx; accepted xx)

**Accepted in *J. Fluid Mech.* (2024).**

The nonlinear evolution of free-stream vortical disturbances entrained in the entrance region of a circular pipe is investigated using asymptotic and numerical methods. Attention is focused on the low-frequency disturbances that induce streamwise elongated structures. A pair of vortical modes with opposite azimuthal wavenumbers is used to model the free-stream disturbances. Their amplitude is assumed to be intense enough for nonlinear interactions to occur inside the pipe. The formation and evolution of the perturbation flow are described by the nonlinear unsteady boundary-region equations in the cylindrical coordinate system, derived and solved herein for the first time. Matched asymptotic expansions are employed to construct appropriate initial conditions and the initial-boundary value problem is solved numerically by a marching procedure in the streamwise direction. Numerical results show the stabilising effect of nonlinearity on the intense algebraic growth of the disturbances and an increase of the wall-shear stress due to the nonlinear interactions. A parametric study is carried out to evince the effect of the Reynolds number, the streamwise and azimuthal wavelengths, and the radial length scale of the inlet disturbance on the nonlinear flow evolution. Elongated pipe-entrance nonlinear structures (EPENS) occupying the whole pipe cross-section are discovered. EPENS with  $h$ -fold rotational symmetry comprise  $h$  high-speed streaks positioned near the wall, and  $h$  low-speed streaks centred around the pipe core. These distinct structures display a striking resemblance to nonlinear travelling waves found numerically and observed experimentally in fully developed pipe flow. Good agreement of our mean-flow and root mean square data with experimental measurements is obtained.

**Key words:**

## 1. Introduction

As one of the most long-standing problems in fluid dynamics, stability and transition in pipe flow have puzzled engineers and scientists since the prominent experimental work of Reynolds (1883). Due to wide industrial applications, engineers have aimed to design efficient and durable pipeline systems by estimating the conditions under which the pipe flow is laminar or turbulent. This objective is driven by the large difference in pressure gradient

† Email address for correspondence: p.ricco@sheffield.ac.uk

34 required to drive laminar and turbulent flows in a pipe. Scientists have also been intrigued by  
35 the enigmatic physical mechanisms behind the instability and transition phenomena observed  
36 in experiments.

37 Earlier investigations of pipe flow date back to the independent studies of Hagen (1839)  
38 and Poiseuille (1844), where the linear relationship between pressure drop and volume flow  
39 rate for laminar flow was obtained. This relationship is now known as the Hagen-Poiseuille  
40 law, which holds only sufficiently downstream where the flow is fully developed, i.e. the  
41 velocity distribution is independent of the streamwise coordinate and its profile is parabolic.  
42 Near the pipe inlet, the velocity field varies in the streamwise direction and the terminologies  
43 developing pipe flow and pipe entrance flow are adopted. Considerable research effort has  
44 been focused on the stability and transition of the fully developed region, but much less  
45 attention has been devoted to the flow in the entrance region of the pipe. In this paper, we  
46 thus aim to investigate how free-stream vortical disturbances are entrained in the entrance  
47 region of a circular pipe and how the induced disturbances grow and evolve nonlinearly  
48 inside the pipe.

### 49 1.1. *Fully developed pipe flow*

50 The stability and transition of fully developed laminar pipe flow cannot be explained by the  
51 classical linear stability theory because the parabolic profile is stable to infinitesimally small  
52 disturbances. The reader is referred to Rayleigh (1892), Sexl (1927), Pekeris (1948), Corcos  
53 & Sellars (1959) and Gill (1965) for theoretical studies, and to Davey & Drazin (1969),  
54 Crowder & Dalton (1971), Garg & Rouleau (1972), Salwen & Grosch (1972) and Meseguer  
55 & Trefethen (2003) for numerical studies. However, transition in pipe flow is usually observed  
56 in experiments at moderate Reynolds numbers. This discrepancy has led to the inclusion of  
57 nonlinear effects in the study of pipe-flow stability. Weakly nonlinear theory was first applied  
58 independently by Davey & Nguyen (1971) and Itoh (1977), but the results contradicted  
59 each other. Davey & Nguyen (1971) reported that fully developed pipe flow was unstable  
60 to small but finite axisymmetric centre-mode disturbances when the disturbance amplitude  
61 exceeded a critical value, while the flow was found to be stable by Itoh (1977). The problem  
62 was reexamined by Davey (1978), who suggested that neither of those results was reliable.  
63 Direct numerical simulations performed by Patera & Orszag (1981) failed to find any finite-  
64 amplitude axisymmetric equilibria and suggested that the use of weakly nonlinear theory  
65 away from the neutral stability curve may be invalid. Smith & Bodonyi (1982) identified  
66 neutral disturbances of finite amplitude by employing the nonlinear critical layer theory.

67 The research interest then shifted from solving the eigenvalue problem established by  
68 the modal stability theory to the temporal initial value problem pertaining to the non-  
69 modal stability theory. Since the linear stability theory captures the long-time disturbance  
70 behaviour but overlooks the short-time behaviour (Kerswell 2005; Schmid 2007), at short  
71 times, disturbances may experience algebraic transient growth before the ultimate exponential  
72 decay (e.g., Böberg & Brösa 1988). One related approach is to identify the optimal disturbance  
73 that achieves the maximum transient energy growth. Studies on transient growth in time  
74 have revealed that optimal disturbances have a vanishing streamwise wavenumber and a  
75 unity azimuthal wavenumber (Bergström 1992; Schmid & Henningson 1994; O'Sullivan &  
76 Breuer 1994). Bergström (1993) and Schmid & Henningson (1994) also extended the work to  
77 disturbances with small but non-zero streamwise wavenumber. The spatial transient growth  
78 has been reported by Tumin (1996) and Reshotko & Tumin (2001). Stationary disturbances  
79 were found to exhibit a more significant amplification than non-stationary ones (Reshotko  
80 & Tumin 2001). Optimal disturbances provide the upper bound for the possible energy  
81 amplification, which is optimised over all possible initial conditions.

82 Faisst & Eckhardt (2003) and Wedin & Kerswell (2004) independently discovered

83 nonlinear travelling waves in pipe flow for the first time, which were later observed in  
84 the experiments of Hof *et al.* (2004) and Hof *et al.* (2005). Inspired by these results, the  
85 nonlinear dynamical system approach has become a valuable tool in the last two decades  
86 (Eckhardt *et al.* 2007; Avila *et al.* 2023). From the perspective of dynamical theory, all initial  
87 conditions of the pipe-flow system that ultimately converge to the laminar state form the basin  
88 of attraction of the laminar state. Transition occurs when the initial conditions are outside  
89 of this basin boundary. The nonlinear non-modal stability theory describes the dynamics of  
90 finite disturbances within and beyond the basin boundary (Kerswell *et al.* 2014; Kerswell  
91 2018). Optimisation methods have been utilised within this nonlinear theory to compute the  
92 so-called minimal seed (Pringle & Kerswell 2010; Pringle *et al.* 2012), i.e. the disturbance  
93 with the smallest energy for turbulence to occur. The interested reader is referred to Kerswell  
94 (2018) for an exhaustive review.

95

### 1.2. Pipe-entrance flow

96 The absence of linear instability in fully developed pipe flow directed interest to the flow  
97 in the developing entrance region. As the uniform flow enters the pipe inlet, a laminar  
98 boundary layer grows along the wall. One can then expect this pipe-entrance boundary layer  
99 to be linearly unstable. Research efforts first focused on the computation of the velocity and  
100 pressure distributions of this base flow (Langhaar 1942; Hornbeck 1964; Sparrow *et al.* 1964;  
101 Christiansen & Lemmon 1965).

102 The first temporal stability analysis of the pipe entrance flow was performed by Tatsumi  
103 (1952) by using a boundary-layer model that revealed the linear instability of the flow  
104 subjected to axisymmetric disturbances. The same problem was investigated numerically by  
105 Huang & Chen (1974a) and generalised to non-axisymmetric disturbances (Huang & Chen  
106 1974b; Shen *et al.* 1976) and spatially unstable disturbances (Gupta & Garg 1981; Garg  
107 1981; Garg & Gupta 1981; Garg 1983). Considerable discrepancies were observed among  
108 the results obtained in these studies, which may be attributed to the varying accuracies in  
109 the calculation of the laminar base flow (da Silva & Moss 1994). da Silva & Moss (1994)  
110 reexamined this stability problem with improved accuracy, obtaining good agreement with  
111 results by Gupta & Garg (1981). The critical Reynolds number based on the pipe radius was  
112 approximately 10 000 in both studies.

113 Although these studies focused on the stability of flow profiles at different streamwise  
114 locations in the pipe entrance, the receptivity problem - i.e. how entrained free-stream  
115 disturbances excite instability in the entrance region - was not considered. This problem is,  
116 however, of central importance because, as even remarked by Reynolds (1883), the pipe inlet  
117 disturbances have a significant effect on the stability and laminar-turbulent transition of the  
118 pipe-entrance flow. By controlling the disturbance level at the pipe inlet, the flow studied by  
119 Reynolds (1883) was maintained laminar up to Reynolds numbers ranging from 2000 to 13  
120 000. This number was further increased to 100 000 in the experiments of Pfenniger (1961).

121 Given the importance of the inlet perturbations, it is thus surprising that only a limited  
122 number of studies exist on this problem. In the experiments of Sarpkaya (1975), disturbances  
123 were introduced on the surface of the pipe entrance, and the occurrence of instability was  
124 confirmed. The reported critical Reynolds number was much lower than that estimated by  
125 theoretical studies, which may be ascribed to the finite-amplitude disturbances induced in  
126 the entrance flow. The dynamics of localised turbulence, i.e. puffs and slugs, was studied  
127 in the experimental work of Wagnanski & Champagne (1973), where the disturbances were  
128 introduced at the pipe inlet using a honeycomb, an orifice plate and a circular disk. Wagnanski  
129 *et al.* (1975) further investigated the propagation of turbulent puffs initiated by an impulsive  
130 disturbance at the entrance region. The experimental study of Zanoun *et al.* (2009) focused

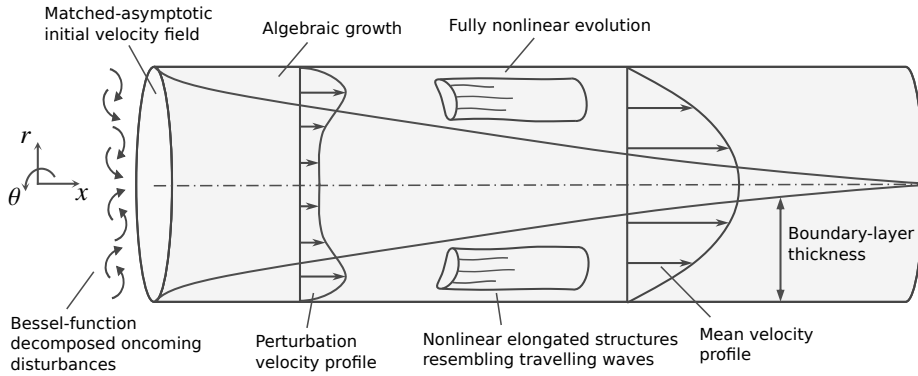


Figure 1: Schematic of the entrance region of a pipe (not to scale).

131 on the effect of the inlet flow conditions on the flow transition in pipe and channel flows.  
 132 Different transition Reynolds numbers were measured at different streamwise positions.

133 Direct numerical simulations were conducted by Wu *et al.* (2015) and Wu *et al.* (2020)  
 134 to investigate the flow transition to fully developed turbulence triggered by localised inlet  
 135 disturbances. In Wu *et al.* (2015), the fully developed parabolic laminar velocity profile was  
 136 chosen as the inlet base flow in most cases, and the plug flow was utilised in one case. The  
 137 most intense inlet disturbances required to trigger transition pertained to the latter case.

138 Under the small-amplitude assumption, Ricco & Alvarenga (2022) performed the first  
 139 theoretical study of the entrainment of free-stream vortical disturbances in the pipe entrance.  
 140 Their interest was in how these disturbances are affected by the pipe confinement, and on  
 141 how they grow and develop downstream. The perturbation flow at the pipe inlet was obtained  
 142 by a matched asymptotic composite solution between a Bessel function vortical flow in the  
 143 pipe core and a boundary-layer flow near the pipe wall. A streamwise-elongated streaky flow  
 144 formed within the base-flow boundary layer and evolved towards the pipe centreline farther  
 145 downstream. A good agreement between the computed velocity profiles and the available  
 146 experimental data was found when the measured free-stream disturbances were weak.

147

### 1.3. Objectives

148 We investigate the entrainment of flow disturbances into the entrance of a circular pipe, and  
 149 the downstream growth and evolution of the induced nonlinear vortical disturbances along the  
 150 entrance region. The oncoming disturbances are physically realistic, i.e. they can be generated  
 151 at the pipe inlet in a laboratory. The nonlinear boundary-region equations are derived in the  
 152 cylindrical geometry for the first time, and solved numerically by marching downstream. Our  
 153 study is the nonlinear extension of Ricco & Alvarenga (2022), and the first theoretical study  
 154 of the entrainment and downstream evolution of finite-amplitude disturbances in the entrance  
 155 region of a circular pipe.

156 In §2, the scaling and assumptions are presented, together with the mathematical formu-  
 157 lation and numerical procedures. Numerical results are discussed in §3. A summary and  
 158 conclusions are given in §4.

## 159 2. Mathematical formulation and numerical procedures

160 We consider a circular pipe of radius  $R^*$  described by a cylindrical coordinate system  
 161  $\{x^*, r^*, \theta\}$ , where  $x^*$  and  $r^*$  are the streamwise and radial directions, and  $\theta$  is the azimuthal  
 162 angle. The pipe inlet is located at  $x^* = 0$ , while the pipe axis and the pipe wall are at  $r^* = 0$

163 and  $r^* = R^*$ , respectively. The superscript  $*$  refers to dimensional quantities hereafter. A  
 164 schematic of the flow is shown in figure 1.

165 A pressure-driven incompressible flow is assumed to enter the pipe with a uniform velocity  
 166  $U_\infty^*$  at  $x^* = 0$ . Superimposed on the oncoming flow are small-amplitude gust-type vortical  
 167 fluctuations that can be modelled by a Fourier–Bessel series with Fourier expansions in  $x^*$ ,  $\theta$   
 168 and time  $t^*$ , and a Bessel expansion in  $r^*$ . A pair of vortical modes with the same frequency  $f^*$   
 169 (and hence the same streamwise wavenumber  $k_x^*$ ), but opposite azimuthal wavenumbers  $\pm m_0$ ,  
 170 is considered ( $m_0 \geq 0$  is taken without losing generality). The circumferential wavelength  
 171 of the free-stream gust at the pipe radius,  $\lambda^* = 2\pi R^*/m_0$ , is chosen as the reference length.  
 172 The velocities and time are normalised by  $U_\infty^*$  and  $\lambda^*/U_\infty^*$ , respectively, while the pressure  
 173  $p^*$  is normalised by  $\rho^* U_\infty^{*2}$ , where  $\rho^*$  is the density of the fluid.

174 Following Ricco & Alvarenga (2022), a single pair of free-stream gusts is passively  
 175 advected by  $U_\infty^*$  and expressed as

$$176 \quad \mathbf{u} - \{1, 0, 0\} = \epsilon \left\{ \hat{\mathbf{u}}_{+,m_0}^\infty e^{im_0\theta} + \hat{\mathbf{u}}_{-,m_0}^\infty e^{-im_0\theta} \right\} e^{ik_x(x-t)} + \text{c.c.}, \quad (2.1)$$

177 where

$$178 \quad \hat{\mathbf{u}}_{\pm,m_0}^\infty(r;l) = \left\{ \hat{u}_{m_0}^\infty J_{m_0}(r_0), \frac{\hat{v}_{m_0}^\infty J_{m_0}(r_0)}{r_0}, \frac{\mp i \hat{w}_{m_0}^\infty J'_{m_0}(r_0)}{\xi_{m_0,l}} \right\} = \mathcal{O}(1). \quad (2.2)$$

179 Here,  $\mathbf{u} = \{u, v, w\}$  corresponds to the velocity components in the  $x$ ,  $r$  and  $\theta$  directions,  $\epsilon \ll 1$   
 180 is a measure of the amplitude of the disturbances, the quantities  $\{\hat{u}_{m_0}^\infty, \hat{v}_{m_0}^\infty, \hat{w}_{m_0}^\infty\} = \mathcal{O}(1)$  are  
 181 complex,  $J_{m_0}$  is the Bessel function of the first kind of order  $m_0$ ,  $r_0 = r\xi_{m_0,l}/2R$  with  $\xi_{m_0,l}$   
 182 being the  $l$ th zero of the Bessel function  $J_{m_0}$ , and c.c. denotes the complex conjugate. The  
 183 notations  $m_0$  and  $r_0$  correspond to  $m$  and  $\bar{r}$  in Ricco & Alvarenga (2022). A similar expansion  
 184 of the free-stream vortical disturbances has been used in Ricco *et al.* (2011) and Marensi  
 185 *et al.* (2017) for flat-plate boundary layers, Marensi & Ricco (2017) for concave boundary  
 186 layers, and Ricco & Alvarenga (2021) for a channel flow. The expansion (2.1)–(2.2) is a  
 187 model of free-stream vortical disturbances that could be realised in a laboratory by a grid of  
 188 vibrating ribbons, a polar equivalent of the careful receptivity studies of Dietz (1999) and  
 189 Borodulin *et al.* (2021).

190 Our focus is on oncoming disturbances with a long streamwise wavelength (i.e. low  
 191 frequency), i.e.  $k_x \ll 1$ , which have been experimentally demonstrated to be the most likely  
 192 to penetrate into a boundary layer and form streamwise-elongated structures (Matsubara &  
 193 Alfredsson 2001). Under the low-frequency assumption, the continuity equation of the gust  
 194 disturbances becomes

$$195 \quad \xi_{m_0,l} \hat{v}_{m_0}^\infty + m_0 \hat{w}_{m_0}^\infty = 0, \quad (2.3)$$

196 where  $\partial u / \partial x = \mathcal{O}(k_x) \ll 1$  has been neglected.

197 As the oncoming flow enters the pipe, a boundary layer develops on the pipe wall. As  
 198 the flow evolves downstream, the boundary-layer thickness becomes comparable with the  
 199 azimuthal wavelength  $\lambda^*$  at  $x = \mathcal{O}(Re_\lambda)$ , where  $Re_\lambda = U_\infty^* \lambda^* / \nu^* \gg 1$ , and  $\nu^*$  is the kinematic  
 200 viscosity of the fluid. A distinguished scaling is  $k_x = \mathcal{O}(Re_\lambda^{-1})$ , and the two slow variables  
 201 scaled by  $k_x$  are  $\bar{t} = k_x t = \mathcal{O}(1)$  and  $\bar{x} = k_x x = \mathcal{O}(1)$ . In this region, viscous–diffusion  
 202 effects in the radial and azimuthal directions are comparable. The flow can be described by  
 203 the nonlinear boundary-region equations (Ricco *et al.* 2011), written and solved herein in  
 204 cylindrical coordinates for the first time. The linear counterpart of these equations, obtained  
 205 for the turbulent Reynolds number  $r_t = \epsilon Re_\lambda \ll 1$ , was derived and solved in Ricco &  
 206 Alvarenga (2022) for studying the growth of small-amplitude disturbances. The current  
 207 research relaxes the linear assumption because  $r_t = \mathcal{O}(1)$ . Nonlinear interactions are thus  
 208 taken into account.

## 2.1. Governing equations

209 The boundary-region equations are derived from the incompressible Navier-Stokes equations

$$211 \quad \nabla \cdot \mathbf{u} = 0, \quad (2.4)$$

$$212 \quad \frac{\partial \mathbf{u}}{\partial t} + (\mathbf{u} \cdot \nabla) \mathbf{u} = -\nabla p + \frac{1}{Re_\lambda} \nabla^2 \mathbf{u}. \quad (2.5)$$

213 The velocity  $\mathbf{u}$  and the pressure  $p$  are decomposed into the laminar base flow and the  
215 perturbation flow, namely

$$216 \quad \begin{aligned} \{\mathbf{u}, p\} &= \{U, P\} + \{\tilde{\mathbf{u}}, \tilde{p}\} \\ &= \{U(\bar{x}, r), k_x V(\bar{x}, r), 0, P(\bar{x})\} + r_t \left\{ \tilde{u}, k_x \tilde{v}, k_x \tilde{w}, \frac{k_x}{Re_\lambda} \tilde{p} + \Gamma(\bar{x}) \right\}, \end{aligned} \quad (2.6)$$

217 where the perturbation flow is expressed as a Fourier series in  $\theta$  and  $t$ :

$$218 \quad \{\tilde{u}, \tilde{v}, \tilde{w}, \tilde{p}, \Gamma\} = \sum_{m,n=-\infty}^{\infty} \{\hat{u}_{m,n}, \hat{v}_{m,n}, \hat{w}_{m,n}, \hat{p}_{m,n}, \hat{\Gamma}_{m,n}\} e^{im\theta + in\bar{t}}. \quad (2.7)$$

219 The pressure correction  $\Gamma(\bar{x})$  ensures that the mass flow rate is conserved at each streamwise  
220 location and time instant as the modes  $\hat{u}_{0,n}$  are generated by the nonlinear interactions.  
221 Therefore,  $\hat{\Gamma}_{m,n} \neq 0$  only if  $m = 0$ . As the physical quantities are real, the Hermitian property  
222 applies, i.e.

$$223 \quad (\hat{q}_{m,n})_{c.c.} = \hat{q}_{-m,-n}, \quad (2.8)$$

224 where  $\hat{q}_{m,n}$  represents any Fourier coefficient  $\{\hat{u}_{m,n}, \hat{v}_{m,n}, \hat{w}_{m,n}, \hat{p}_{m,n}, \hat{\Gamma}_{m,n}\}$  in (2.7).

225 Substituting (2.6) and (2.7) into the full Navier-Stokes equations (2.4)–(2.5), and taking  
226 the limits  $k_x^{-1}, Re_\lambda \rightarrow \infty$  with  $\mathcal{F} = k_x Re_\lambda = \mathcal{O}(1)$  leads to the boundary-layer equations  
227 governing the laminar base flow  $\{U, V, P\}$  and to the unsteady nonlinear boundary-region  
228 equations governing the perturbation flow  $\{\hat{u}_{m,n}, \hat{v}_{m,n}, \hat{w}_{m,n}, \hat{p}_{m,n}, \hat{\Gamma}_{m,n}\}$ .

229 The laminar boundary-layer equations read (Hornbeck 1964)

$$230 \quad \frac{\partial U}{\partial \bar{x}} + \frac{V}{r} + \frac{\partial V}{\partial r} = 0, \quad (2.9)$$

$$231 \quad U \frac{\partial U}{\partial \bar{x}} + V \frac{\partial U}{\partial r} = -\frac{dP}{d\bar{x}} + \frac{1}{\mathcal{F}} \left( \frac{1}{r} \frac{\partial U}{\partial r} + \frac{\partial^2 U}{\partial r^2} \right). \quad (2.10)$$

232 Equation (2.9) and (2.10) are solved together with the conservation of mass flow rate at each  
233 streamwise location,

$$234 \quad \int_0^R U r dr = \frac{R^2}{2}, \quad (2.11)$$

235 and are subject to the no-slip and no-penetration conditions at the wall and the symmetry  
236 conditions at the pipe axis:

$$237 \quad r = R : \quad U = V = 0, \quad (2.12)$$

$$238 \quad r = 0 : \quad \frac{\partial U}{\partial r} = 0, \quad V = 0. \quad (2.13)$$

239 The initial condition is obtained by a matched asymptotic combination of the Blasius flow

241 near the pipe wall and an inviscid flow around the pipe core (Ricco & Alvarenga 2022),

$$\begin{aligned}
 U(x, r) = & \frac{dF}{d\eta} - \frac{\beta i^{1/2}}{2\sqrt{2\pi}Re_\lambda^{1/2}} \int_{-\infty+i\gamma}^{+\infty+i\gamma} \frac{e^{i\zeta x}}{\zeta^{1/2} I_1(\zeta R)} \left[ \frac{I_1(\zeta r)}{\zeta r} + I_1'(\zeta r) \right] d\zeta + \\
 & \frac{\beta i^{1/2}}{2\sqrt{2\pi}Re_\lambda^{1/2}} \int_{-\infty+i\gamma}^{+\infty+i\gamma} \frac{e^{i\zeta x}}{\zeta^{1/2}} \left[ \frac{I_1'(\zeta R)}{I_1(\zeta R)} + \frac{1}{\zeta R} \right] d\zeta, \quad x \ll 1
 \end{aligned} \tag{2.14}$$

243 where  $\eta = (R - r)(Re_\lambda/2x)^{1/2}$ ,  $F$  satisfies the Blasius equation  $F''' + FF'' = 0$ , the prime  
 244 denotes differentiation,  $\beta = \lim_{\eta \rightarrow \infty} (\eta - F) = 1.217\dots$ ,  $I_1$  is the modified Bessel function of  
 245 the first kind, and  $\gamma \in \mathbb{R} < 0$ . Equations (2.9)–(2.11), supplemented by conditions (2.12)–  
 246 (2.14), are solved by an improved version of the numerical scheme of Hornbeck (1964). A  
 247 detailed description of the numerical procedure is provided in the supplementary material  
 248 S1 of Ricco & Alvarenga (2022). The numerical results are discussed in §4.1 of Ricco &  
 249 Alvarenga (2022).

250 The perturbation-flow unsteady nonlinear boundary-region equations are as follows.

251 The continuity equation is

$$\frac{\partial \hat{u}_{m,n}}{\partial \bar{x}} + \frac{\hat{v}_{m,n}}{r} + \frac{\partial \hat{v}_{m,n}}{\partial r} + \frac{im}{r} \hat{w}_{m,n} = 0. \tag{2.15}$$

254 The  $x$ -momentum equation is

$$\begin{aligned}
 & \left( in + \frac{\partial U}{\partial \bar{x}} + \frac{m^2}{\mathcal{F}r^2} \right) \hat{u}_{m,n} + U \frac{\partial \hat{u}_{m,n}}{\partial \bar{x}} + \left( V - \frac{1}{\mathcal{F}r} \right) \frac{\partial \hat{u}_{m,n}}{\partial r} + \hat{v}_{m,n} \frac{\partial U}{\partial r} - \\
 & \frac{1}{\mathcal{F}} \frac{\partial^2 \hat{u}_{m,n}}{\partial r^2} + \frac{d\hat{\Gamma}_{0,n}}{d\bar{x}} = r_t \hat{\mathcal{X}}_{m,n}.
 \end{aligned} \tag{2.16}$$

257 The  $r$ -momentum equation is

$$\begin{aligned}
 & \left( in + \frac{\partial V}{\partial r} + \frac{m^2 + 1}{\mathcal{F}r^2} \right) \hat{v}_{m,n} + U \frac{\partial \hat{v}_{m,n}}{\partial \bar{x}} + \hat{u}_{m,n} \frac{\partial V}{\partial \bar{x}} + \left( V - \frac{1}{\mathcal{F}r} \right) \frac{\partial \hat{v}_{m,n}}{\partial r} + \\
 & \frac{1}{\mathcal{F}} \frac{\partial \hat{p}_{m,n}}{\partial r} - \frac{1}{\mathcal{F}} \frac{\partial^2 \hat{v}_{m,n}}{\partial r^2} + \frac{2im}{\mathcal{F}r^2} \hat{w}_{m,n} = r_t \hat{\mathcal{Y}}_{m,n}.
 \end{aligned} \tag{2.17}$$

260 The  $\theta$ -momentum equation is

$$\begin{aligned}
 & \left( in + \frac{V}{r} + \frac{m^2 + 1}{\mathcal{F}r^2} \right) \hat{w}_{m,n} + U \frac{\partial \hat{w}_{m,n}}{\partial \bar{x}} + \left( V - \frac{1}{\mathcal{F}r} \right) \frac{\partial \hat{w}_{m,n}}{\partial r} + \frac{im}{\mathcal{F}r} \hat{p}_{m,n} - \\
 & \frac{1}{\mathcal{F}} \frac{\partial^2 \hat{w}_{m,n}}{\partial r^2} - \frac{2im}{\mathcal{F}r^2} \hat{v}_{m,n} = r_t \hat{\mathcal{Z}}_{m,n}.
 \end{aligned} \tag{2.18}$$

262 The right-hand sides of the momentum equations (2.16)–(2.18) denote the nonlinear terms

$$\left. \begin{aligned}
 \hat{\mathcal{X}}_{m,n} &= - \left( \frac{\partial \widehat{uu}}{\partial \bar{x}} + \frac{\partial \widehat{uv}}{\partial r} + \frac{\widehat{uv} + im\widehat{uw}}{r} \right)_{m,n}, \\
 \hat{\mathcal{Y}}_{m,n} &= - \left( \frac{\partial \widehat{uv}}{\partial \bar{x}} + \frac{\partial \widehat{vv}}{\partial r} + \frac{\widehat{vv} + im\widehat{vw} - \widehat{wv}}{r} \right)_{m,n}, \\
 \hat{\mathcal{Z}}_{m,n} &= - \left( \frac{\partial \widehat{uw}}{\partial \bar{x}} + \frac{\partial \widehat{vw}}{\partial r} + \frac{im\widehat{ww}}{r} + \frac{2\widehat{vw}}{r} \right)_{m,n},
 \end{aligned} \right\} \tag{2.19}$$

264 where  $\hat{\cdot}$  indicates Fourier transformed quantities. In the limit  $r_t \ll 1$ , the linearised boundary-  
 265 region equations of Ricco & Alvarenga (2022) are recovered. The pressure correction  $\hat{\Gamma}_{0,n}$   
 266 becomes a further unknown variable for  $m = 0$ , and one more condition is thus required  
 267 to solve the system. Analogous to (2.11) for the base-flow problem, this condition is the  
 268 conservation of mass flow rate at each instant in time and at each streamwise location. As  
 269 discussed in Appendix A, this condition is expressed as

$$270 \quad \int_0^R \hat{u}_{0,n} r dr = 0. \quad (2.20)$$

271 Since the partial differential system (2.15)–(2.20) is parabolic in the streamwise direction  
 272 and elliptic in the radial and azimuthal directions, appropriate initial and boundary conditions  
 273 are needed. These conditions are presented in §2.2. Further treatment of (2.15)–(2.20) is  
 274 carried out in §2.3 for different values of  $m$ . The numerical procedures are discussed in §2.4.

## 275 2.2. Initial and boundary conditions

276 While the streamwise velocity of the induced disturbances acquires an order-one amplitude  
 277 at  $\bar{x} = O(1)$ , the velocity fluctuations near the pipe inlet are of small amplitude  $O(\epsilon)$  and  
 278 nonlinear effects can therefore be neglected there. Hence the initial conditions derived by  
 279 Ricco & Alvarenga (2022) can be used. Comparison of the velocity expansions (2.6) here  
 280 and (2.6) in Ricco & Alvarenga (2022) leads to the relations

$$281 \quad \{\hat{u}_{m_0,-1}, \hat{v}_{m_0,-1}\} = \frac{1}{Re_\lambda} \left\{ \frac{im_0}{k_x} \bar{u}_x + \bar{u}_x^{(0)}, \frac{im_0}{k_x} \bar{u}_r + \bar{u}_r^{(0)} \right\}, \quad (2.21)$$

282 where  $\bar{u}_x$ ,  $\bar{u}_r$ ,  $\bar{u}_x^{(0)}$  and  $\bar{u}_r^{(0)}$  are given by the analytical expressions (3.25)–(3.27) and  
 283 (3.32) in Ricco & Alvarenga (2022). The azimuthal velocity  $\hat{w}_{m_0,-1}$  can be found through  
 284 the continuity equation (2.15), with  $\hat{u}_{m_0,-1}$  and  $\hat{v}_{m_0,-1}$  given by (2.21). For the opposite  
 285 wavenumber  $m = -m_0$ , the same streamwise and radial components but opposite azimuthal  
 286 component are derived

$$287 \quad \{\hat{u}_{-m_0,-1}, \hat{v}_{-m_0,-1}, \hat{w}_{-m_0,-1}\} = \{\hat{u}_{m_0,-1}, \hat{v}_{m_0,-1}, -\hat{w}_{m_0,-1}\}. \quad (2.22)$$

288 It also occurs that

$$289 \quad \hat{u}_{m,n} = \hat{v}_{m,n} = \hat{w}_{m,n} = 0 \quad \text{for } (m,n) \neq (\pm m_0, -1). \quad (2.23)$$

290 Since the streamwise derivative of  $\hat{p}_{m,n}$  is negligible in the  $x$ -momentum equation (2.16)  
 291 under the low-frequency assumption, no initial condition for  $\hat{p}_{m,n}$  is required.

292 In the radial direction, equations (2.15)–(2.20) are subjected to the no-slip and no-  
 293 penetration conditions at the wall ( $r = R$ ),

$$294 \quad \hat{u}_{m,n} = \hat{v}_{m,n} = \hat{w}_{m,n} = 0, \quad (2.24)$$

295 while the boundary conditions at the pipe axis ( $r = 0$ ) are

$$296 \quad \left. \begin{aligned} \hat{u}'_{m,n} = 0, \hat{v}_{m,n} = 0, \hat{w}_{m,n} = 0, \hat{p}'_{m,n} = 0, & \quad \text{for } m = 0, \\ \hat{u}_{m,n} = 0, \hat{v}'_{m,n} = 0, \hat{w}'_{m,n} = 0, \hat{p}_{m,n} = 0, & \quad \text{for } |m| = 1, \\ \hat{u}_{m,n} = 0, \hat{v}_{m,n} = 0, \hat{w}_{m,n} = 0, \hat{p}_{m,n} = 0, & \quad \text{for } |m| \geq 2, \end{aligned} \right\} \quad (2.25)$$

297 where the prime indicates the derivative with respect to  $r$ . Conditions (2.25) are derived  
 298 following Batchelor & Gill (1962), Tuckerman (1989) and Lewis & Bellan (1990), who  
 299 studied the physical constraints on the coefficients of Fourier expansions in cylindrical  
 300 coordinates (refer also to supplementary material S3 of Ricco & Alvarenga (2022)).



### 2.3. Initial-boundary value problems

301

302 For convenience of the numerical calculations, the nonlinear boundary-region equations  
 303 (2.15)–(2.20), together with the initial conditions (2.21)–(2.23) and the boundary conditions  
 304 (2.24)–(2.25), are solved in different forms according to the value of  $m$ .

305

306

307

Case I For the components with  $m \neq 0$ , the pressure  $\hat{p}_{m,n}$  and the azimuthal velocity  
 $\hat{w}_{m,n}$  can be eliminated from (2.15)–(2.19) as in Ricco & Alvarenga (2022). The resulting  
 equations read

$$\left(in + \frac{\partial U}{\partial \bar{x}} + \frac{m^2}{\mathcal{F}r^2}\right)\hat{u}_{m,n} + \left(V - \frac{1}{\mathcal{F}r}\right)\frac{\partial \hat{u}_{m,n}}{\partial r} + U\frac{\partial \hat{u}_{m,n}}{\partial \bar{x}} - \frac{1}{\mathcal{F}}\frac{\partial^2 \hat{u}_{m,n}}{\partial r^2} + \frac{\partial U}{\partial r}\hat{v}_{m,n} = r_t \hat{\mathcal{X}}_{m,n}, \quad (2.26)$$

308

$$\begin{aligned} & \widehat{V}\hat{v}_{m,n} + \widehat{V}_r\frac{\partial \hat{v}_{m,n}}{\partial r} + \widehat{V}_x\frac{\partial \hat{v}_{m,n}}{\partial \bar{x}} + \widehat{V}_{rr}\frac{\partial^2 \hat{v}_{m,n}}{\partial r^2} + \widehat{V}_{xr}\frac{\partial^2 \hat{v}_{m,n}}{\partial \bar{x}\partial r} + \widehat{V}_{rrr}\frac{\partial^3 \hat{v}_{m,n}}{\partial r^3} + \widehat{V}_{xrr}\frac{\partial^3 \hat{v}_{m,n}}{\partial \bar{x}\partial r^2} + \\ & \widehat{V}_{rrrr}\frac{\partial^4 \hat{v}_{m,n}}{\partial r^4} + \widehat{U}\hat{u}_{m,n} + \widehat{U}_r\frac{\partial \hat{u}_{m,n}}{\partial r} + \widehat{U}_x\frac{\partial \hat{u}_{m,n}}{\partial \bar{x}} + \widehat{U}_{rr}\frac{\partial^2 \hat{u}_{m,n}}{\partial r^2} + \widehat{U}_{xr}\frac{\partial^2 \hat{u}_{m,n}}{\partial \bar{x}\partial r} + \end{aligned}$$

311

$$\widehat{U}_{xrr}\frac{\partial^3 \hat{u}_{m,n}}{\partial \bar{x}\partial r^2} = r_t\frac{r^2}{m^2}\frac{\partial^2 \hat{\mathcal{X}}_{m,n}}{\partial \bar{x}\partial r} + r_t\hat{\mathcal{Y}}_{m,n} + \frac{ir_t}{m}\frac{\partial (r\hat{\mathcal{Z}}_{m,n})}{\partial r}, \quad (2.27)$$

312

313

314

where the coefficients  $\widehat{V}, \widehat{V}_r, \widehat{V}_x, \dots, \widehat{U}_{xrr}$  are given in Appendix B. Only the initial and  
 boundary conditions for  $\{\hat{u}_{m,n}, \hat{v}_{m,n}\}$  are needed in this case. The initial conditions are given  
 in (2.21)–(2.23). The boundary conditions are

315

$$\hat{u}_{m,n} = \hat{v}_{m,n} = \hat{v}'_{m,n} = 0, \quad \text{at } r = R \quad (2.28)$$

316 and

317

$$\left. \begin{aligned} \hat{u}_{m,n} = 0, \quad \hat{v}_{m,n} = 0, \quad \hat{v}''_{m,n} = 0, \quad \text{for } |m| = 1, \\ \hat{u}_{m,n} = 0, \quad \hat{v}_{m,n} = 0, \quad \hat{v}'_{m,n} = 0, \quad \text{for } |m| = 2, \\ \hat{u}_{m,n} = 0, \quad \hat{v}_{m,n} = 0, \quad \hat{v}'_{m,n} = 0, \quad \text{for } |m| > 2, \end{aligned} \right\} \text{at } r = 0. \quad (2.29)$$

318

319

320

321

322

323

324

325

At the pipe wall,  $r = R$ , the last condition  $\hat{w}_{m,n} = 0$  in (2.24) is replaced by  $\hat{v}'_{m,n} = 0$  in (2.28),  
 which is obtained by inserting (2.24) into the continuity equation (2.15). At the pipe axis,  
 $r = 0$ , the conditions for  $\hat{w}$  and  $\hat{w}'$  in (2.25) for different  $m$  are replaced following the physical  
 constraints proposed by Batchelor & Gill (1962), Khorrami *et al.* (1989), Tuckerman (1989)  
 and Lewis & Bellan (1990), as discussed in supplementary material S3 of Ricco & Alvarenga  
 (2022). The azimuthal velocity  $\hat{w}_{m,n}$  can be obtained *a posteriori* from the continuity equation  
 and the pressure  $\hat{p}_{m,n}$  can then be calculated from either the  $r$ -momentum equation (2.17)  
 or the  $\theta$ -momentum equation (2.18).

326

327

328

Case II For the components with  $m = 0$ , the pressure  $\hat{p}_{0,n}$  appears only in the  $r$ -momentum  
 equation (2.17). The three velocity components  $\{\hat{u}_{0,n}, \hat{v}_{0,n}, \hat{w}_{0,n}\}$  can be solved by the  
 continuity,  $x$ - and  $\theta$ -momentum equations,

329

$$\frac{\partial \hat{u}_{0,n}}{\partial \bar{x}} + \frac{\hat{v}_{0,n}}{r} + \frac{\partial \hat{v}_{0,n}}{\partial r} = 0, \quad (2.30)$$

330

$$\left(in + \frac{\partial U}{\partial \bar{x}}\right)\hat{u}_{0,n} + U\frac{\partial \hat{u}_{0,n}}{\partial \bar{x}} + \left(V - \frac{1}{\mathcal{F}r}\right)\frac{\partial \hat{u}_{0,n}}{\partial r} + \hat{v}_{0,n}\frac{\partial U}{\partial r} - \frac{1}{\mathcal{F}}\frac{\partial^2 \hat{u}_{0,n}}{\partial r^2} + \frac{d\hat{\Gamma}_{0,n}}{d\bar{x}} = r_t \hat{\mathcal{X}}_{0,n}, \quad (2.31)$$

331

$$\left(in + \frac{V}{r} + \frac{1}{\mathcal{F}r^2}\right)\hat{w}_{0,n} + U\frac{\partial \hat{w}_{0,n}}{\partial \bar{x}} + \left(V - \frac{1}{\mathcal{F}r}\right)\frac{\partial \hat{w}_{0,n}}{\partial r} - \frac{1}{\mathcal{F}}\frac{\partial^2 \hat{w}_{0,n}}{\partial r^2} = r_t \hat{\mathcal{Z}}_{0,n}, \quad (2.32)$$

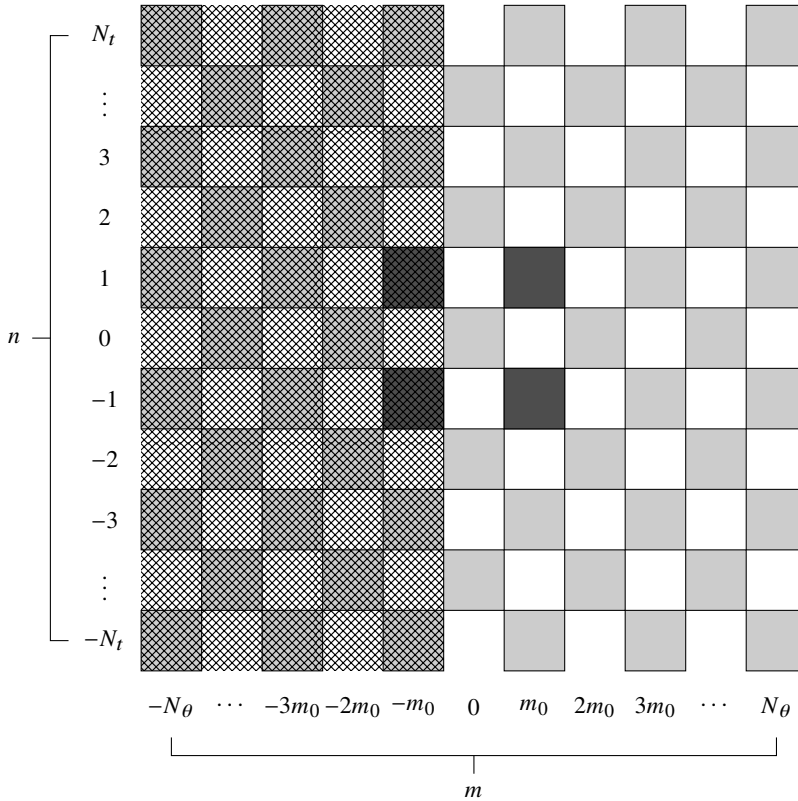


Figure 2: Sketch of Fourier modes induced by a pair of free-stream vortical modes. Dark grey squares: forcing modes  $(\pm m_0, \pm 1)$ . Light grey squares: nonlinearly generated modes. The modes in the shaded area are computed through the Hermitian property (2.8).

332 together with (2.20) for the conservation of the mass flow rate, as discussed in §2.1. The  
 333 pressure  $\hat{p}_{0,n}$  is computed *a posteriori* by integrating the  $r$ -momentum equation (2.17). The  
 334 boundary conditions for the velocity components and the pressure are given in (2.24) and  
 335 (2.25) for  $m = 0$ . The initial conditions for  $\hat{u}_{0,n}, \hat{v}_{0,n}, \hat{w}_{0,n}$  are null.

336

#### 2.4. Numerical procedures

337 The initial-boundary value problems are solved by marching in the streamwise direction  
 338  $\bar{x}$ . The governing equations for both cases are discretised by second-order finite-difference  
 339 schemes employing a one-sided backward uniform grid along  $\bar{x}$  and a central-difference  
 340 uniform grid along  $r$ . The discretised system of case I forms a block tridiagonal matrix and  
 341 is solved at each  $\bar{x}$  location by a standard block tridiagonal matrix algorithm (Cebeci 2002).  
 342 For case II, the composite trapezoidal rule is used for the calculation of the integral (2.20).  
 343 Since the velocity components and the pressure gradient are computed simultaneously, the  
 344 block tridiagonal structure of the matrix is lost. A novel modified block tridiagonal matrix  
 345 algorithm is utilised to accelerate the numerical solution of this system, as discussed in  
 346 Appendix C.

347 The computation of the nonlinear terms on the right-hand sides of the momentum equations  
 348 is refined by a predictor–corrector method at each  $\bar{x}$  location. In the predictor step, the initial  
 349 approximation of the nonlinear terms uses the results at the previous  $\bar{x}$  location to treat the  
 350 discretised nonlinear system explicitly. The velocity computed from the predictor step is used

351 to improve the initial guess in the corrector step. This iteration is repeated until a convergence  
 352 criterion is fulfilled. An under-relaxation method is used to accelerate this procedure. At each  
 353 iteration, nonlinear terms are calculated using the pseudo-spectral method, in which first the  
 354 Fourier coefficients of the velocity components are transformed to the physical space to carry  
 355 out the multiplications, and the products are then transformed back to the spectral space.  
 356 The aliasing error is eliminated by employing the 3/2 rule, which avoids the spurious energy  
 357 cascade from the unresolved high-frequency modes into the resolved low-frequency ones.  
 358 As the Hermitian property is applied for the azimuthal angle  $\theta$ , only the Fourier modes  
 359 with non-negative indices  $m$  need to be calculated. The modes with negative  $m$  indices are  
 360 evaluated through (2.8). Figure 2 shows a sketch of the Fourier modes induced by a pair  
 361 of free-stream vortical modes  $(\pm m_0, \pm 1)$ . Only the modes with  $m = \pm m_0, \pm 2m_0, \pm 3m_0, \dots$   
 362 and  $n = \pm 1, \pm 2, \pm 3, \dots$  can be generated by nonlinearity. Fourier modes are truncated at  
 363  $m = \pm N_\theta$  and  $n = \pm N_t$  for the azimuthal wavenumber and the frequency, respectively.  
 364 Resolution checks show that the use of  $N_t = 6$ ,  $N_\theta = 12$  is sufficient to capture the nonlinear  
 365 effects induced by the free-stream forcing modes with wavenumber  $m_0 = 2$ . For larger  $m_0$ , a  
 366 correspondingly larger value of  $N_\theta$  is necessary (e.g.  $N_\theta = 18$  for  $m_0 = 3$ ).

### 367 3. Results

368 In the analysis of the flow, the kinetic energy of the free-stream gust averaged over the pipe  
 369 cross-section is kept constant:

$$\begin{aligned}
 370 \quad \mathcal{E}_{m_0,l}^{gust} &= \frac{1}{2\pi R^2} \int_0^{2\pi} \int_0^R \left( |\tilde{u}|^2 + |\tilde{v}|^2 + |\tilde{w}|^2 \right) r dr d\theta \\
 371 \quad &= \frac{4\epsilon^2}{R^2} \int_0^R \left[ \left( \hat{u}_{m_0}^\infty J_{m_0}(r_0) \right)^2 + \left( \frac{\hat{v}_{m_0}^\infty J_{m_0}(r_0)}{r_0} \right)^2 + \left( \frac{\hat{v}_{m_0}^\infty J'_{m_0}(r_0)}{m_0} \right)^2 \right] r dr, \quad (3.1) \\
 372
 \end{aligned}$$

373 where the gust velocity components in (2.2) have been used. The relation (2.3) is utilised to  
 374 eliminate  $\hat{w}_{m_0}^\infty$  from (3.1). Without losing generality,  $\hat{u}_{m_0}^\infty$  is fixed at 1 in our analysis. With  
 375  $m_0$  and  $l$  specified, the only parameter to be determined is  $\hat{v}_{m_0}^\infty$ , which is found by equating  
 376  $\mathcal{E}_{m_0,l}^{gust}$  to  $\mathcal{E}_{1,1}^{gust}$ , the perturbation energy for  $m_0 = l = 1$  and  $\hat{v}_{m_0}^\infty = 1$ . A similar approach was  
 377 adopted in Schmid & Henningson (1994), where the maximum energy amplification was  
 378 computed over initial conditions with the same energy norm. The intensity used to measure  
 379 the fluctuation level of the gust is defined as  $Tu = \sqrt{(2/3)\mathcal{E}_{m_0,l}^{gust}}$ .

380 In §2, the circumferential wavelength of the gust  $\lambda^*$  at the pipe radius is selected as the  
 381 reference length in order to relate our asymptotic analysis to the boundary-layer analysis of  
 382 Leib *et al.* (1999), while the numerical results are presented herein with quantities rescaled  
 383 by the pipe radius  $R^*$ , i.e.  $\mathbf{u} = \mathbf{u}(x_R, r_R; k_{x,R}, Re_R, l, m_0)$ , where  $x_R = x^*/R^*$ ,  $r_R = r^*/R^*$ ,  
 384  $k_{x,R} = k_x^* R^*$  and  $Re_R = U_\infty^* R^*/\nu^*$ . We focus on the nonlinear evolution of disturbances in  
 385 the parameter space  $k_{x,R} \ll 1$  and  $Re_R < 10000$ , where Tollmien–Schlichting waves are not  
 386 present (refer to figure 2 of Ricco & Alvarenga (2022)). In our reference case,  $k_{x,R} = 0.02$ ,  
 387  $Re_R = 1000$ ,  $l = 3$ ,  $m_0 = 2$  and  $\epsilon = 0.05$  (i.e.  $Tu \approx 4\%$ ).

388 The intensity of the disturbances is monitored by the root mean square (r.m.s.) of the  
 389 streamwise velocity fluctuation,  $u_{rms}$  (Pope 2000, p.687):

$$390 \quad u_{rms} = r_t \left( \sum_{m=-N_\theta}^{N_\theta} \sum_{n=-N_t}^{N_t} |\hat{u}_{m,n}|^2 \right)^{1/2}, \quad n \neq 0. \quad (3.2)$$

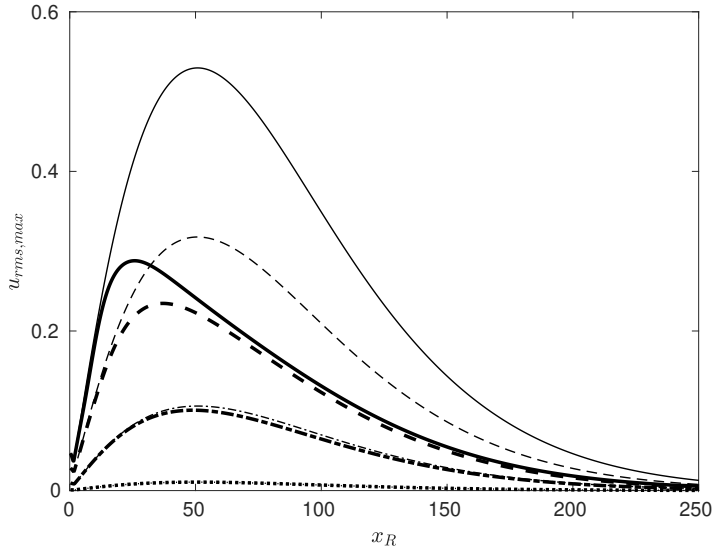


Figure 3: Thick lines: nonlinear streamwise development of  $u_{rms,max}$  for  $\epsilon = 0.001$  (dotted), 0.01 (dash-dotted), 0.03 (dashed), 0.05 (solid). Thin lines: linear solutions rescaled by corresponding  $\epsilon$  value.

391

### 3.1. Effect of flow parameters

392 Figure 3 shows the nonlinear streamwise development of the maximum  $u_{rms}$  (thick lines),  
 393 i.e.  $u_{rms,max} = \max_{x_R} u_{rms}$ , for different values of  $\epsilon = 0.001, 0.01, 0.03, 0.05$  (i.e.  $Tu \approx$   
 394  $0.08\%, 0.8\%, 2.4\%, 4\%$ ). The linear results are rescaled by the corresponding  $\epsilon$  value and  
 395 displayed by thin lines. The linear and nonlinear solutions overlap when the amplitude  
 396 of the oncoming disturbance is small ( $\epsilon = 0.001$ ) due to the weak nonlinear interaction,  
 397 while nonlinear effects become more intense as  $\epsilon$  increases. When  $\epsilon = 0.03$  and  $0.05$ ,  
 398 the nonlinear growth of the disturbances agrees with the corresponding linear growth only  
 399 near the pipe inlet, and becomes much slower farther downstream. The peak location of  
 400 the nonlinear profiles moves upstream as  $\epsilon$  increases, and the peak amplitude is lower than  
 401 the corresponding linear one. This latter result indicates the stabilising role of nonlinearity  
 402 and the overprediction of the linear results. The maximum amplification of the nonlinear  
 403 solution for  $\epsilon = 0.05$  is, for example, only 54.4% of that of the linear solution. Sufficiently  
 404 downstream, both linear and nonlinear disturbances experience monotonic decay and tend to  
 405 zero. The stabilising effect of nonlinearity has already been noticed, for example, by Ricco  
 406 *et al.* (2011) and Marensi & Ricco (2017) for the development of the streaks in boundary  
 407 layers over flat and concave plates, respectively.

408 Figure 4 shows the effects of different parameters,  $k_{x,R}$ ,  $Re_R$ ,  $l$  and  $m_0$ , on the nonlinear  
 409 development of  $u_{rms,max}$  along the streamwise direction  $x_R$ . In figure 4(a), the overlap of  
 410 profiles at the smaller  $x_R$  indicates that the streamwise wavenumber  $k_{x,R}$  has no influence  
 411 on the initial growth of the disturbances. The profiles for  $k_{x,R} = 0.001$  and  $0.02$  are almost  
 412 indistinguishable for the whole extent  $x_R$  of the pipe. By further increasing  $k_{x,R}$  up to  $0.1$ ,  
 413 the amplitude of  $u_{rms,max}$  reaches a lower peak and decays at a larger rate.

414 Figure 4(b) displays the influence of the Reynolds number  $Re_R$  ranging from 1000 to  
 415 2500. The independence of the initial growth of the disturbance is also found by changing  
 416  $Re_R$ . For  $Re_R \leq 2000$ , the evolution features one maximum after the initial growth, while,  
 417 for  $Re_R > 2000$ , two maxima are observed. Farther downstream, the disturbance decays at a  
 418 slower rate as  $Re_R$  increases.

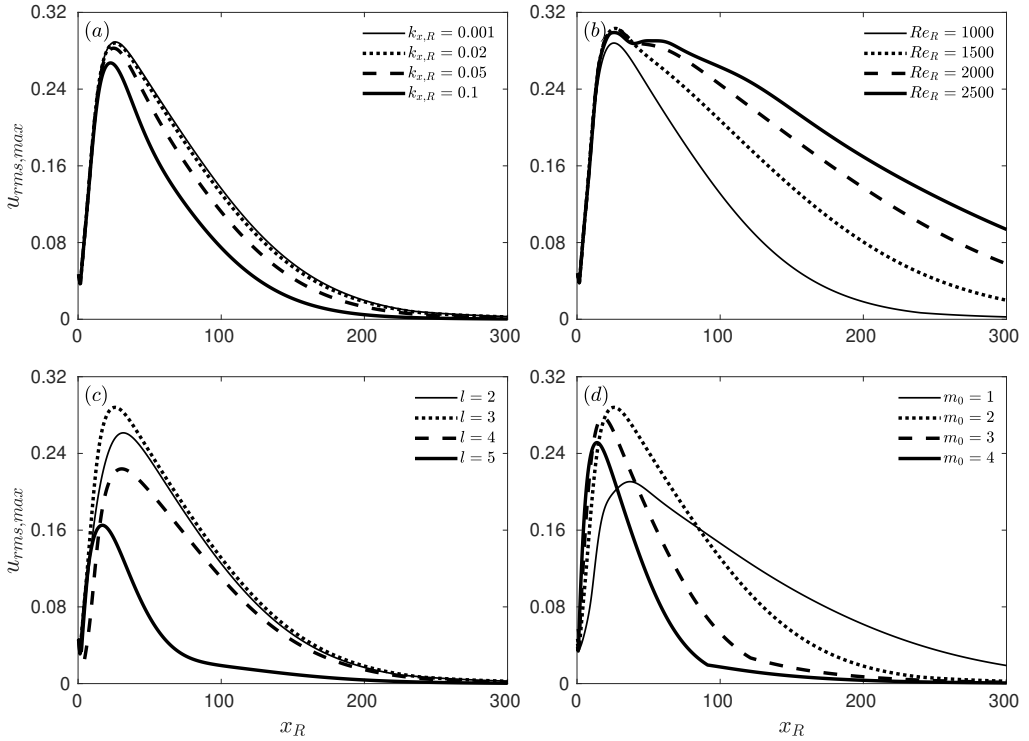


Figure 4: Effects of different parameters on the streamwise development of  $u_{rms,max}$ . (a) Streamwise wavenumber  $k_{x,R}$ ; (b) Reynolds number  $Re_R$ ; (c) parameter  $l$  characterising the radial length scale; (d) azimuthal wavenumber  $m_0$ .

419 Figure 4(c) shows how the change of the parameter  $l$  affects the downstream development  
 420 of  $u_{rms,max}$ . As the characteristic radial scale of the oncoming disturbances is defined by the  
 421  $l$ th zero of the Bessel function, i.e.  $\xi_{m_0,l}$  in expansion (2.1)–(2.2), a large  $l$  value corresponds  
 422 to a small characteristic radial length scale, as shown in figure 20(a) of Ricco & Alvarenga  
 423 (2022). The most intense growth occurs for  $l = 3$ .

424 The effect of the azimuthal wavenumber  $m_0$  is shown in figure 4(d). Increasing  $m_0$  induces  
 425 a more intense initial growth. Different from the linear case where the maximum growth is  
 426 found at wavenumber  $m_0 = 3$  (Ricco & Alvarenga 2022), the nonlinear disturbances grow  
 427 the most for  $m_0 = 2$ . A similar finding was reported by Reshotko & Tumin (2001) in the  
 428 analysis of spatial transient growth in fully developed pipe flow, where non-stationary optimal  
 429 disturbances were obtained for azimuthal wavenumbers larger than 1. The smaller  $m_0$ , the  
 430 more the disturbances persist downstream.

### 431 3.2. Results for a representative case

432 The representative case with  $k_{x,R} = 0.02$ ,  $Re_R = 1000$ ,  $l = 3$ ,  $m_0 = 2$ ,  $\epsilon = 0.05$  is analysed.  
 433 Figures 5(a) and 5(b) show the profiles of  $u_{rms}$  at different streamwise locations. The  
 434 maximum of  $u_{rms}$  appears close to the wall for locations near the pipe inlet, and gradually  
 435 shifts towards the centreline as  $x_R$  increases. Its amplitude increases with  $x_R$  up to  $x_R \approx 26$ ,  
 436 after which a monotonic decrease occurs downstream. Near the pipe inlet, a significant  
 437 disturbance growth is obtained in the region close to the pipe core ( $0.1 < r_R < 0.5$ ) where  
 438 the base flow is largely inviscid. The disturbances in boundary layers subjected to free-stream  
 439 turbulence show a similar growth in the outer region (figure 2(c) of Matsubara & Alfredsson

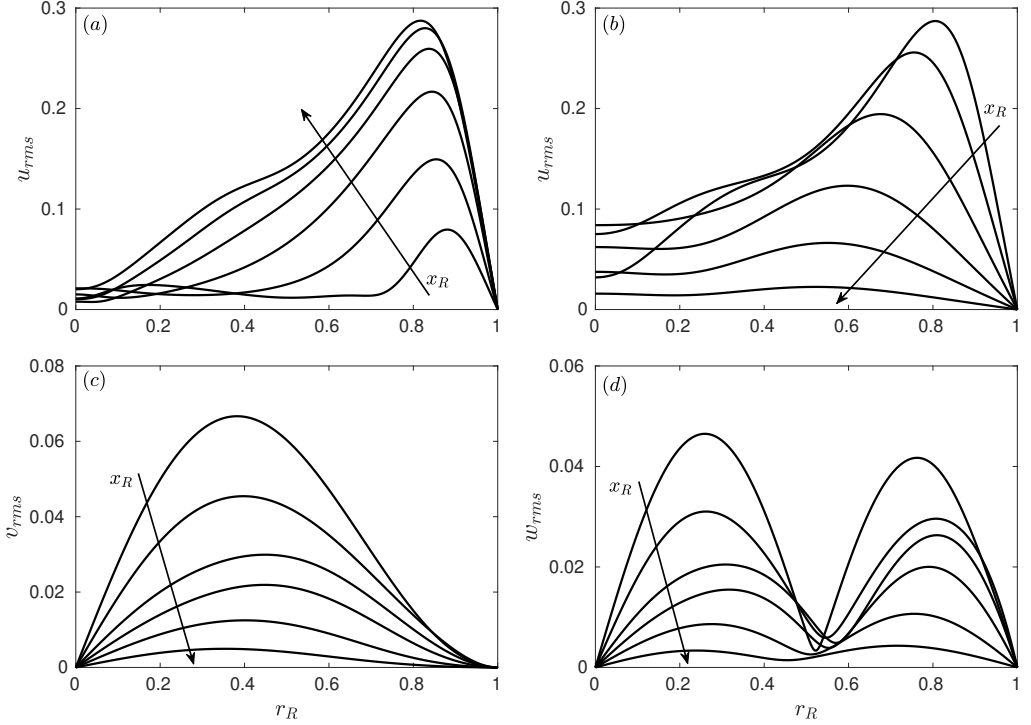


Figure 5: Profiles of  $u_{rms}$ ,  $v_{rms}$  and  $w_{rms}$  at different streamwise locations: (a) growing  $u_{rms}$  at  $x_R = 4, 8, 12, 16, 20, 24$ ; (b) decaying  $u_{rms}$  at  $x_R = 28, 44, 70, 104, 140, 191$ . (c, d)  $v_{rms}$  and  $w_{rms}$  at  $x_R = 4, 12, 20, 28, 44, 70$ . Arrows indicate the increasing  $x_R$  direction.

440 (2001) and figure 10 of Ricco *et al.* (2011)). This growth does not occur in the linearised case,  
 441 where the disturbances are confined in the near-wall region (figure 15 of Ricco & Alvarenga  
 442 (2022)). The streamwise developments of  $v_{rms}$  and  $w_{rms}$  are shown in figures 5(c) and 5(d).  
 443 The amplitudes of  $v_{rms}$  and  $w_{rms}$  are comparable with that of  $u_{rms}$  close to the pipe inlet,  
 444 while they become much smaller downstream after considerable attenuation.

445 Figure 6 displays the downstream development of the forcing mode  $(m, n) = (2, 1)$  (red  
 446 line) and the nonlinearly generated modes, which are characterised by  $\max_{r_R} |r_t \hat{u}_{m,n}|$ , the  
 447 maximum intensity of  $|r_t \hat{u}_{m,n}|$  at each  $x_R$  location. For the assumed free-stream disturbances  
 448 (2.1), modes  $(m, n)$  and  $(-m, -n)$  have the same amplitude. Modes  $(m, n)$  and  $(-m, -n)$  also  
 449 have the same amplitude because of the Hermitian property (2.8). Therefore, without losing  
 450 generality, only the results for  $m \geq 0$  and  $n \geq 0$  are presented. The mean-flow distortion  $\hat{u}_{0,0}$   
 451 acquires considerable growth shortly downstream of the pipe inlet, overshoots the forcing  
 452 mode  $\hat{u}_{2,1}$  at  $x_R \approx 24.4$ , and becomes dominant downstream. The amplitude of the higher  
 453 harmonics also grows because of the strong nonlinear interaction when  $\epsilon = 0.05$ , and then  
 454 attenuates due to viscous effects. Downstream of  $x_R = 200$ , only the forcing mode  $\hat{u}_{2,1}$ , the  
 455 mean-flow distortion  $\hat{u}_{0,0}$  and the pulsatile mode  $\hat{u}_{0,2}$  still exist. They all decay to zero farther  
 456 downstream.

457 Figure 7 shows the streamwise velocity profiles of the mean-flow distortion  $r_t \hat{u}_{0,0}$ , the  
 458 forcing modes  $r_t |\hat{u}_{2,1}|$  and the higher harmonics  $r_t |\hat{u}_{0,2}|$ ,  $r_t |\hat{u}_{4,0}|$ ,  $r_t |\hat{u}_{4,2}|$  at six different  
 459 streamwise locations,  $x_R = 4, 16, 32, 51, 96, 180$ . The most intense growth is obtained by  
 460  $\max_{r_R} |r_t \hat{u}_{0,0}|$  at  $x_R = 51$  (refer to figure 6). The ordinate axis in 7(a) and 7(f) is stretched

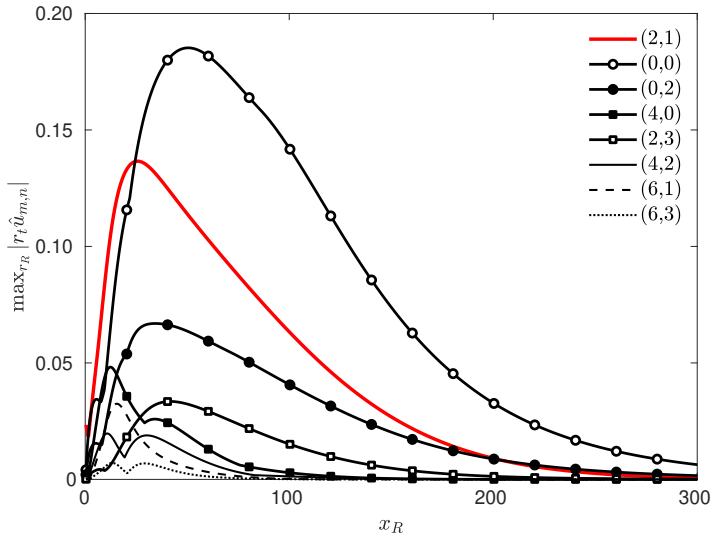


Figure 6: Streamwise development of the forcing mode (red line) and nonlinearly generated modes, characterised by  $\max_{r_R} |r_t \hat{u}_{m,n}|$ .

461 by a factor of 2 for clarity. Significant growth and decay in the velocity amplitude are  
 462 observed for modes  $r_t \hat{u}_{0,0}$ ,  $r_t |\hat{u}_{2,1}|$  and  $r_t |\hat{u}_{0,2}|$  along the pipe entrance. Moreover, the shape  
 463 of velocity profiles changes substantially as the flow evolves downstream. The positive values  
 464 of the mode  $r_t \hat{u}_{0,0}$  near the wall indicate an increase of the wall-shear stress. The second  
 465 harmonics,  $r_t |\hat{u}_{4,0}|$  and  $r_t |\hat{u}_{4,2}|$ , experience considerable attenuation shortly after the initial  
 466 growth and are almost negligible at  $x_R = 96$  and  $180$ .

467 Figure 8 shows the streamwise velocity profiles of the laminar base flow  $U$  (dashed lines)  
 468 and the mean flow  $\bar{U}$  (solid lines), i.e. the velocity averaged in  $t$  and  $\theta$ , at the same streamwise  
 469 locations as those in figure 7. Mathematically, the distorted mean flow  $\bar{U}$  is the sum of the  
 470 laminar base flow and the mean-flow distortion, i.e.  $\bar{U} = U + r_t \hat{u}_{0,0}$ . A significant deviation  
 471 from the laminar base flow is observed in figure 8(d) ( $x_R = 51$ ), where  $\max_{r_R} |r_t \hat{u}_{0,0}|$  reaches  
 472 the maximum growth. In the pipe core region, the profile exhibits a deficit with respect to  
 473 the laminar base flow, while it is larger than the laminar value near the wall. The profiles of  
 474 the mean-flow distortion  $r_t \hat{u}_{0,0}$  shown in figure 7 further explain these velocity deficits and  
 475 surpluses. Positive mean-flow distortion  $r_t \hat{u}_{0,0}$  always exists near the pipe wall, while in the  
 476 pipe core it is positive only near the inlet, and negative farther downstream.

477 Figure 9 displays contour plots of the velocity components  $\tilde{u}$ ,  $\tilde{v}$  and  $\tilde{w}$  (from left to right) at  
 478  $\bar{t} = 0$  and four different streamwise locations  $x_R = 4, 26, 60, 150$  (from top to bottom). These  
 479 plots visualise the formation and evolution of elongated pipe-entrance nonlinear structures  
 480 (EPENS). Near the pipe inlet ( $x_R = 4$ ), the three velocity components are of comparable  
 481 amplitude. The EPENS appear because the streamwise component  $\tilde{u}$  becomes prevalent at  
 482  $x_R = 26$  (attributed to the growth of  $\tilde{u}$  and the attenuation of  $\tilde{v}$  and  $\tilde{w}$ ), where the disturbances  
 483 are most amplified, as shown in figure 3. In contrast to the nonlinear streaks observed in  
 484 transitional boundary-layer flows (Matsubara & Alfredsson 2001) that are confined in the  
 485 near-wall region, these EPENS occupy the entire cross-section with two high-speed streaks  
 486 near the pipe wall, and two low-speed streaks near the pipe core. The twofold rotational  
 487 symmetry featured by these EPENS results from the dominance of the forcing mode  $\hat{u}_{2,1}$   
 488 among all the modes with  $m \neq 0$  (refer to figure 6). The modes with  $m = 0$  are uniform in  
 489 the azimuthal direction. The gradual downstream attenuation after  $x_R = 26$  can be observed

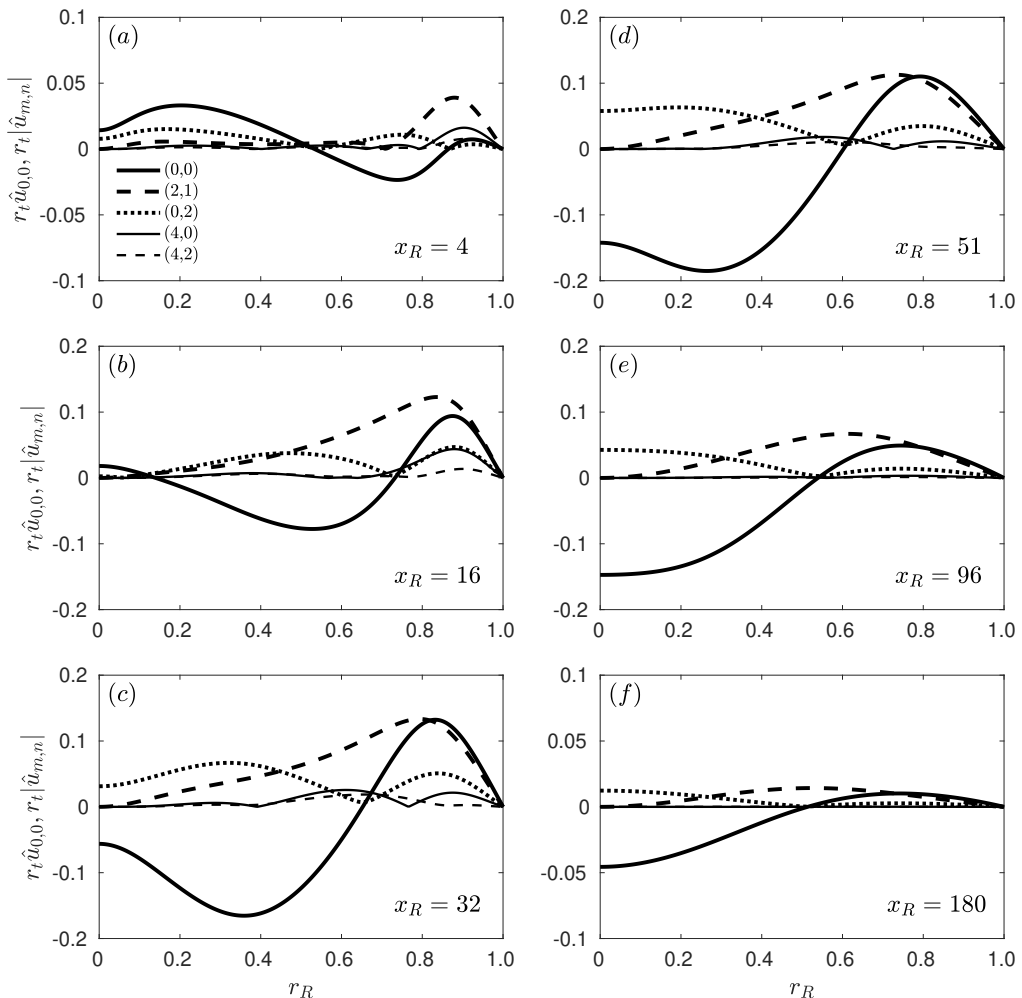


Figure 7: Streamwise velocity profiles of the mean-flow distortion  $r_t \hat{u}_{0,0}$ , forcing modes  $r_t |\hat{u}_{2,1}|$  and second harmonics  $r_t |\hat{u}_{0,2}|$ ,  $r_t |\hat{u}_{4,0}|$ ,  $r_t |\hat{u}_{4,2}|$  at different streamwise locations.

490 in the last two rows of figure 9, corresponding to  $x_R = 60$  and 150. At  $x_R = 60$  and 150,  
 491 the low-speed streaks merge near the pipe core, flanked by the high-speed streaks on their  
 492 sides. Contours of the streamwise velocity  $\tilde{u}$  at  $x_R = 200$  and four different time phases  
 493  $\bar{t} = 0, \pi/4, \pi/2, 3\pi/4$  are shown in figure 10. The radial and azimuthal velocities  $\tilde{v}$  and  $\tilde{w}$  are  
 494  $\mathcal{O}(10^{-5})$  at that location, thus are not shown. The distributions of  $\tilde{u}$  at  $\bar{t} \in [\pi, 2\pi]$  exhibit the  
 495 same features as those at  $\bar{t} \in [0, \pi]$ , but with a rotation of  $90^\circ$  around the pipe axis.

496

### 3.3. Comparison with travelling waves

497 The nonlinear vortical structures evolving along the pipe entrance are now compared with  
 498 travelling waves appearing in fully developed pipe flow. Inspired by the self-sustained  
 499 process proposed by Waleffe (1997), Faisst & Eckhardt (2003) and Wedin & Kerswell  
 500 (2004) discovered three-dimensional travelling waves (TWs) in pipe flow. These nonlinear  
 501 waves consist of streamwise vortices, streaks and streamwise-dependent wavy structures.  
 502 They were also observed experimentally in turbulent puffs and in fully developed turbulence  
 503 by Hof *et al.* (2004). New families of TWs have also been reported in Pringle & Kerswell



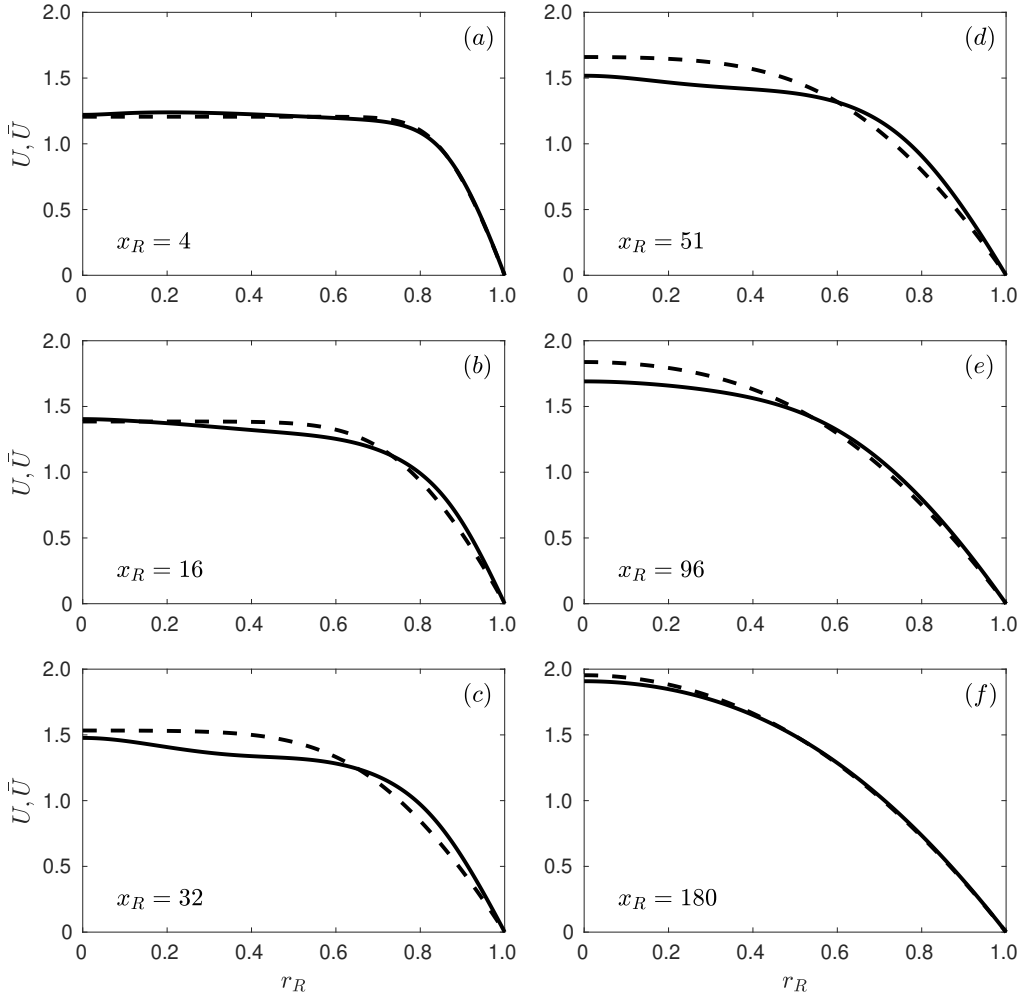


Figure 8: Streamwise velocity profiles of the laminar base flow  $U$  (dashed line) and the distorted mean flow  $\tilde{U} = U + r_1 \hat{u}_{0,0}$  (solid line) at different streamwise locations.

504 (2007) and Pringle *et al.* (2009). These TWs are nonlinear solutions of the Navier–Stokes  
 505 equations and they capture distinct features of coherent structures observed in turbulent pipe  
 506 flow (Graham & Floryan 2021). Willis & Kerswell (2008) suggested that these TWs populate  
 507 an intermediate region between the laminar and turbulent states in phase space. However,  
 508 the physical origin of these TWs has not been discussed and remains unclear.

509 As shown in figure 11, excellent visual agreement occurs between the  $\mathcal{R}_3$ -TW (where  
 510  $\mathcal{R}_h$  represents the  $h$ -fold rotational symmetry) found by Wedin & Kerswell (2004) and the  
 511  $\mathcal{R}_3$ -EPENS at the same Reynolds number,  $Re_R = 900$ . (The Reynolds number based on the  
 512 pipe diameter used in Wedin & Kerswell (2004), Willis *et al.* (2017) and Kerswell & Tutty  
 513 (2007) has been converted to  $Re_R$  herein.) The EPENS are shown at  $x_R = 18$  and  $\bar{t} = 0$ ,  
 514 where  $u_{urm,max}$  attains the largest amplitude. Remarkable agreement is observed for the  
 515 streamwise vortices and the high/low-speed streaks, although the TWs are found in fully  
 516 developed pipe flow while the EPENS exist in the pipe entrance region. Both the  $\mathcal{R}_3$ -TW  
 517 and  $\mathcal{R}_3$ -EPENS have three equispaced low-speed streaks (dark) located towards the centre  
 518 and three equispaced high-speed streaks (light) positioned near the wall. For both sets of

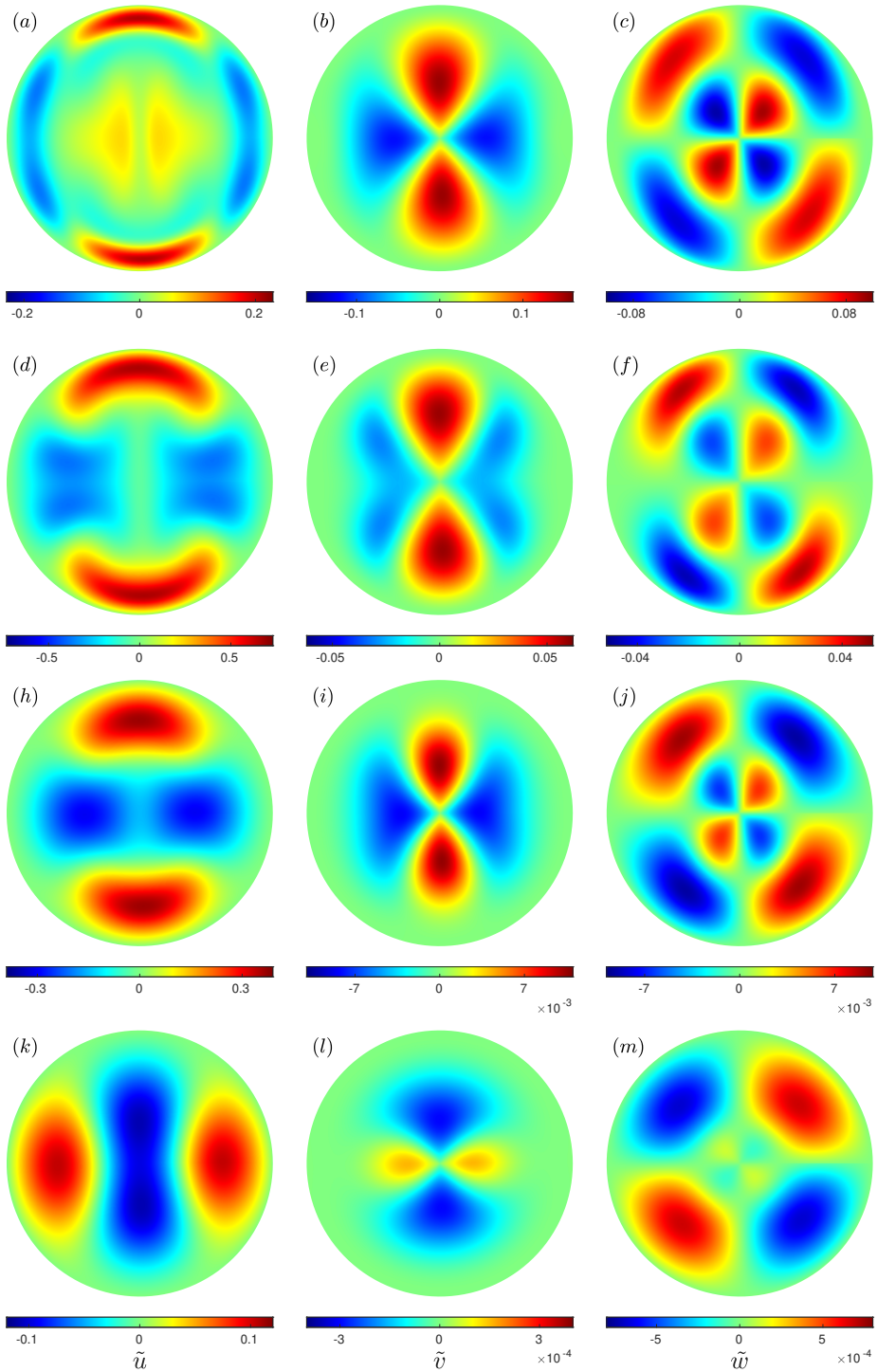


Figure 9: Contours of the velocity components  $\tilde{u}$ ,  $\tilde{v}$  and  $\tilde{w}$  (from left to right) at the time instant  $\tilde{t} = 0$  and four different locations  $x_R = 4, 26, 60, 150$  (from top to bottom), where the red/blue coloured shading indicates velocity faster/slower than the laminar base-flow velocity  $U$ . The same shading is used in figure 10.

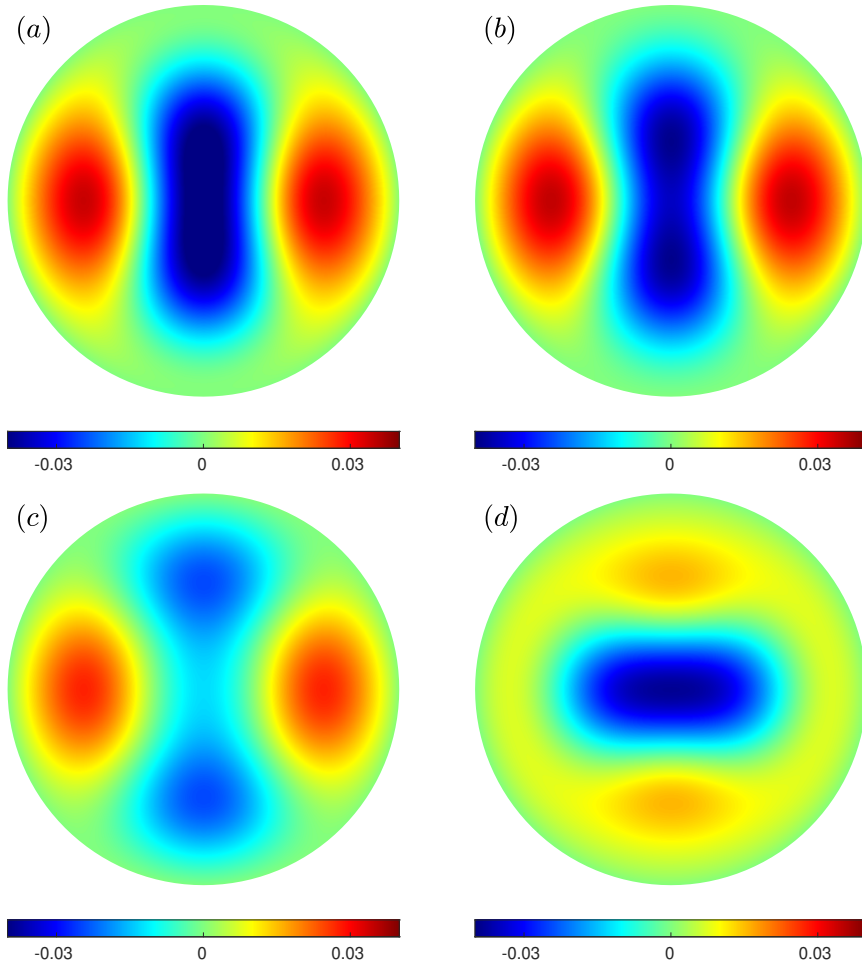


Figure 10: Contours of the streamwise velocity  $\bar{u}$  at the streamwise location  $x_R = 200$  and four different time phases (a)  $\bar{t} = 0$ , (b)  $\bar{t} = \pi/4$ , (c)  $\bar{t} = \pi/2$ , and (d)  $\bar{t} = 3\pi/4$ .

519 nonlinear structures, streamwise vortices are located between adjacent low-speed and high-  
 520 speed streaks, moving fluid towards the pipe axis in correspondence with low-speed streaks  
 521 and wallward where high-speed streaks exist.

522 The TWs originate mathematically from saddle–node bifurcations and are calculated using  
 523 a homotopy approach. However, this numerical method does not explain the physical origin of  
 524 TWs. The method to compute the EPENS instead describes the physical origin of EPENS, i.e.  
 525 the EPENS arise from the algebraic growth, nonlinear interactions and streamwise stretching  
 526 of realistic vortical disturbances convected by the uniform flow approaching and entering the  
 527 pipe inlet. We note that other receptivity mechanisms, such as wall vibration or roughness,  
 528 could also create them. Wedin & Kerswell (2004) found that multiple solution branches  
 529 coexist at higher Reynolds numbers (refer to figure 10 of Wedin & Kerswell (2004)). Besides  
 530 the  $\mathcal{R}_h$  solution shown in figure 11(a), which consists of  $h$  high-speed streaks near the wall,  
 531 Wedin & Kerswell (2004) also discovered solutions with  $2h$  near-wall high-speed streaks in  
 532 other branches. Only EPENS with  $h$  high-speed streaks are instead found in our computations.

533 With figure 11(b) as a reference, computations of EPENS for  $m_0 = 3$  are carried out for  
 534 different  $Re_R$ ,  $k_{x,R}$  and  $l$ . The results are displayed in figure 12 at the locations where the

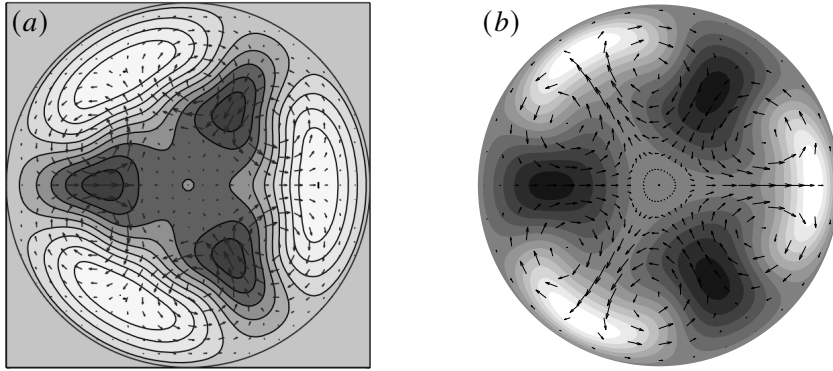


Figure 11: Comparison of velocity fields between the  $\mathcal{R}_3$ -TW and  $\mathcal{R}_3$ -EPENS for  $Re_R = 900$ . The cross-section vectors  $\tilde{v}\mathbf{j} + \tilde{w}\mathbf{k}$  (where  $\mathbf{j}$  and  $\mathbf{k}$  are unit vectors in the radial and azimuthal directions) are indicated by arrows. The streamwise velocity  $\tilde{u}$  is indicated by the shading, where light/dark colour indicates  $\tilde{u}$  faster/slower than the laminar base-flow velocity  $U$ . The same shading is used in figures 12, 13 and 14. (a) The  $\mathcal{R}_3$ -TW found by Wedin & Kerswell (2004). (b) The  $\mathcal{R}_3$ -EPENS calculated at  $x_R = 18$ , where they are most amplified, and  $\bar{t} = 0$  with  $\epsilon = 0.05$ ,  $k_{x,R} = 0.02$ ,  $l = 3$  and  $m_0 = 3$ .

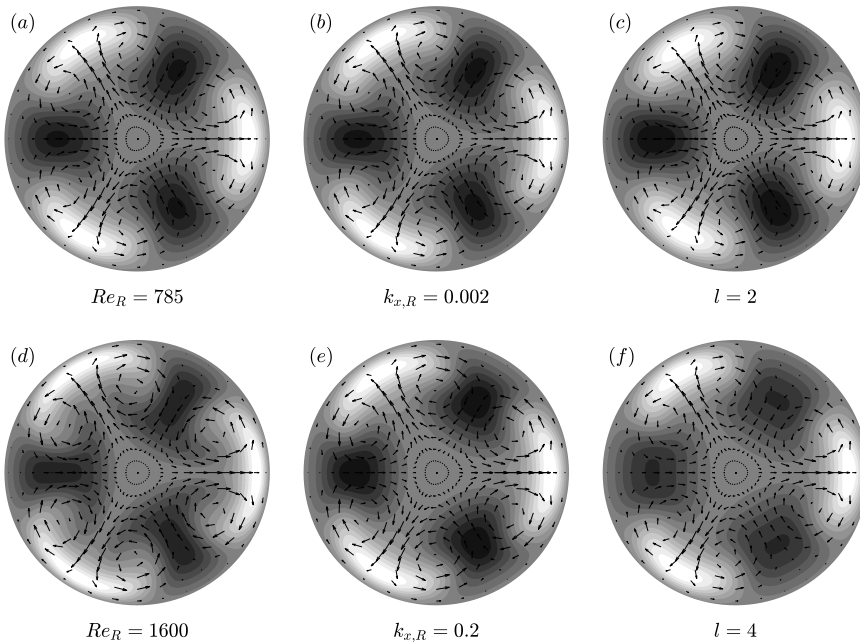


Figure 12: Velocity fields of  $\mathcal{R}_3$ -EPENS at locations where they are most amplified and  $\bar{t} = 0$  for different  $Re_R$ ,  $k_{x,R}$  and  $l$ . Unless otherwise stated, the parameters are  $\epsilon = 0.05$ ,  $Re_R = 900$ ,  $k_{x,R} = 0.02$ ,  $l = 3$  and  $m_0 = 3$ . (a)  $Re_R = 785$ ,  $x_R = 17$ . (b)  $k_{x,R} = 0.002$ ,  $x_R = 18$ . (c)  $l = 2$ ,  $x_R = 22$ . (d)  $Re_R = 1600$ ,  $x_R = 19$ . (e)  $k_{x,R} = 0.2$ ,  $x_R = 15$ . (f)  $l = 4$ ,  $x_R = 20$ .

535 EPENS are most amplified. Figure 11(a) corresponds to solution *a* in figure 10 of Wedin &  
 536 Kerswell (2004), which was used for the branch continuation. This branch was traced down  
 537 to  $Re_R = 785$  and up to  $Re_R = 1600$ . Figures 12(a) and 12(d) show the EPENS calculated  
 538 at these two Reynolds numbers. The similarities in the dominant streaks and vortices of

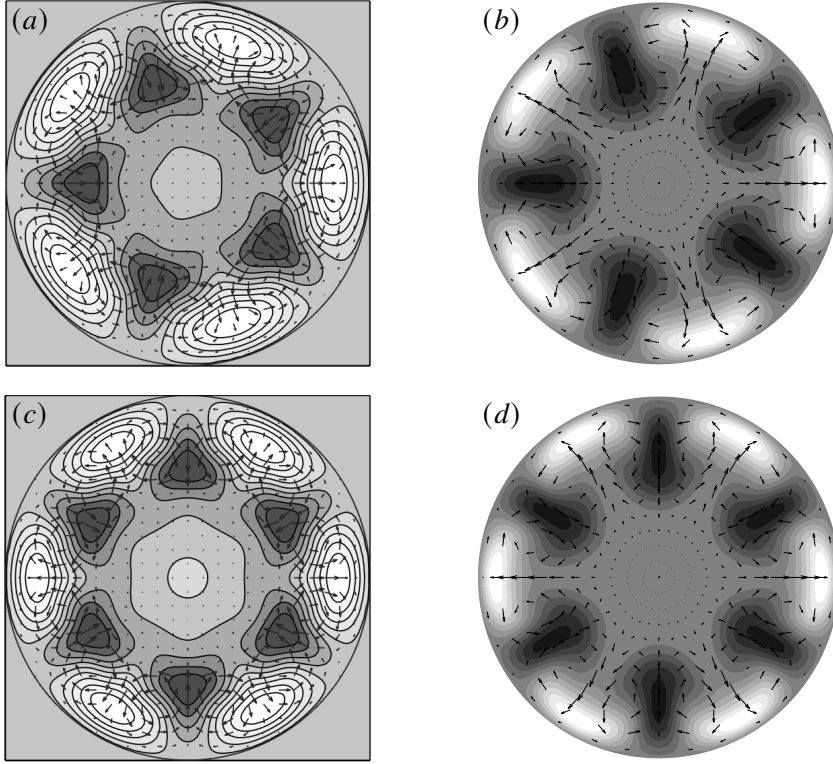


Figure 13: Comparison of velocity fields between TWs and EPENS for rotational symmetries  $\mathcal{R}_5$  at  $Re_R = 1242.75$  and  $\mathcal{R}_6$  at  $Re_R = 1434.5$ . (a, c) The  $\mathcal{R}_5$ - and  $\mathcal{R}_6$ -TW found by Wedin & Kerswell (2004) at their saddle-node bifurcations. (b, d) The  $\mathcal{R}_5$ - and  $\mathcal{R}_6$ -EPENS calculated at  $x_R = 12$  and  $11$ , where they are most amplified, and  $\bar{t} = 0$  for  $\epsilon = 0.05$ ,  $k_{x,R} = 0.02$ ,  $l = 3$ , and  $m_0 = 5, 6$ .

539 EPENS for different  $Re_R$  are observed. As  $Re_R$  increases, the low-speed streaks appear  
 540 slightly narrower along the azimuthal direction, and the high-speed streaks become slightly  
 541 more flattened towards the wall. The close resemblance among TWs pertaining to the same  
 542 branch for different  $Re_R$  was also reported in Wedin & Kerswell (2004). Figures 12(b) and  
 543 12(e) show that varying the frequency by one hundred times has only a minimal impact on  
 544 the EPENS. The robustness of the EPENS is further confirmed in figures 12(b) and 12(e)  
 545 by varying the radial modulation of the inlet perturbation flow, given by the change of the  
 546 parameter  $l$ . Increasing  $l$ , indicating an inlet perturbed flow with a smaller radial length scale,  
 547 has only a mild influence on the EPENS. This result proves that the EPENS are likely to be  
 548 a strong attractor of the dynamical system.

549 Except for the  $\mathcal{R}_3$  symmetry, only TWs at their saddle-node bifurcations are presented for  
 550 other rotational symmetry in Wedin & Kerswell (2004). Among these solutions,  $\mathcal{R}_5$ - and  
 551  $\mathcal{R}_6$ -TWs consist of  $h$  high-speed streaks near the wall, while  $\mathcal{R}_1$ -,  $\mathcal{R}_2$ - and  $\mathcal{R}_4$ -TWs have  
 552  $2h$  high-speed streaks. Remarkable agreement between TWs and EPENS is also obtained  
 553 for the  $\mathcal{R}_5$  and  $\mathcal{R}_6$  rotational symmetries, as reported in figure 13. The EPENS with  $h$ -  
 554 fold rotational symmetry observed downstream is always excited by free-stream vortical  
 555 disturbances with azimuthal wavenumber  $m_0 = h$ . The discovery of  $\mathcal{R}_1$ -TWs, which possess  
 556 no discrete rotational symmetry, was reported in Pringle & Kerswell (2007). These TWs  
 557 are more important than the rotationally symmetric ones because the upper/lower branches  
 558 correspond to much higher/lower wall-shear stress values compared to rotationally symmetric

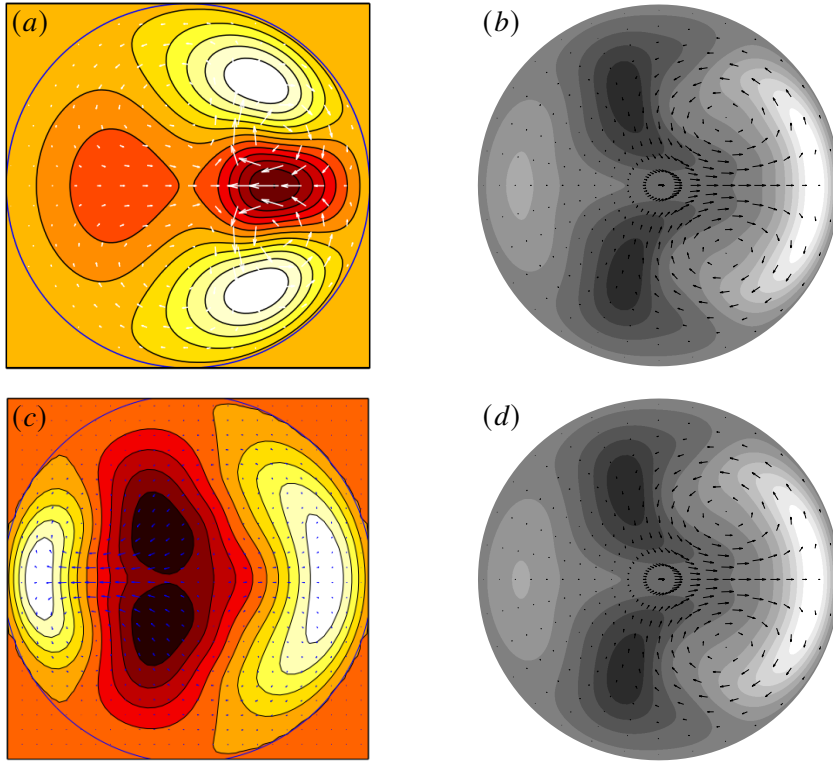


Figure 14: Comparison of velocity fields between the asymmetric TWs and  $\mathcal{R}_1$ -EPENS for  $Re_R = 1450$  (a, b) and 1340 (c, d). (a, c) The asymmetric TWs found by Pringle & Kerswell (2007) and Willis *et al.* (2017), where the white/dark coloured shading indicates  $\tilde{u}$  faster/slower than the laminar base-flow velocity  $U$ . (b, d) The  $\mathcal{R}_1$ -EPENS calculated at  $x_R = 36$ , where they are most amplified, and  $\bar{t} = 0$  with  $\epsilon = 0.05$ ,  $k_{x,R} = 0.02$ ,  $l = 3$ , and  $m_0 = 1$ .

559 ones. Figure 14(a) shows the velocity field of an asymmetric TW of these new families. One  
 560 low-speed streak is centred at half the distance between the wall and the centreline, and is  
 561 surrounded by two high-speed streaks. As shown in figure 14(b), rotationally asymmetric  
 562 EPENS are also found in our calculation when  $m_0 = 1$ . However, they consist of one wide  
 563 near-wall high-speed streak flanked by two low-speed streaks, and one low-intensity high-speed  
 564 streak on the opposite side of the wide high-speed streak. The cross-section velocity  
 565 vector field reveals that counter-rotating streamwise vortices occur between the high-speed  
 566 and the low-speed streaks. Using a feedback control strategy, a new asymmetric TW was  
 567 identified by Willis *et al.* (2017) (figure 14(c)). Good agreement is noted between the streaks  
 568 of their TW and our  $\mathcal{R}_1$ -EPENS at the same Reynolds number, whereas only very weak  
 569 streamwise vortices are found between the wide high-speed streak and low-speed streaks in  
 570 their case.

571 The comparison of streamwise velocity isosurfaces of the  $\mathcal{R}_3$ -TW calculated by Kerswell  
 572 & Tutty (2007) and the  $\mathcal{R}_3$ -EPENS at  $Re_R = 1200$  is also very good, as shown in figure 15,  
 573 where the light and dark shadings denote the streamwise velocity for  $\tilde{u} = 0.3U$  and  $-0.3U$ .  
 574 The  $\mathcal{R}_3$ -TW is displayed versus its wavelength (the diameter of the pipe is used as a reference  
 575 length), while the  $\mathcal{R}_3$ -EPENS is displayed for  $13 < x_R < 17$ . Along these distances, both the  
 576 near-wall high-speed streaks and the low-speed streaks near the pipe core for both the TW  
 577 and EPENS evolve slowly in the streamwise direction.

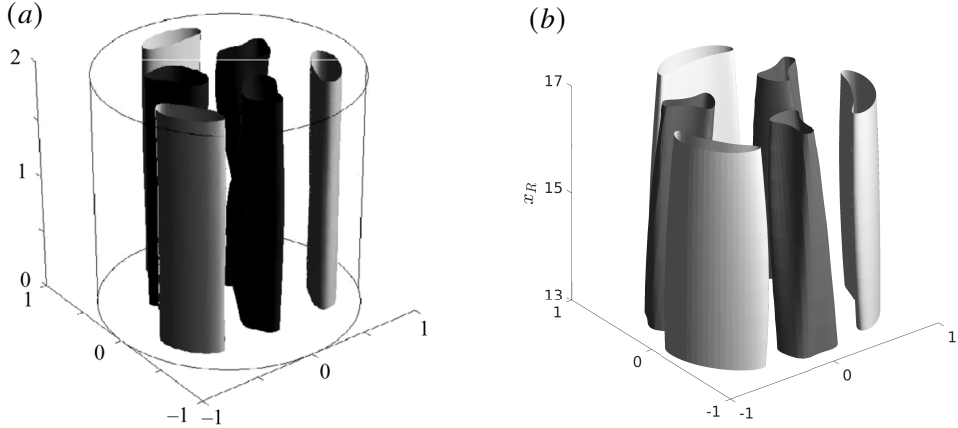


Figure 15: Comparison of streamwise velocity isosurfaces between the  $\mathcal{R}_3$ -TW and  $\mathcal{R}_3$ -EPENS for  $Re_R = 1200$ . The light and dark shading represents the streamwise velocity  $\bar{u}$  that equals  $0.3U$  and  $-0.3U$ . (a) The  $\mathcal{R}_3$ -TW over the wavelength found by Kerswell & Tutty (2007). (b) The  $\mathcal{R}_3$ -EPENS calculated for  $13 \ll x_R \ll 17$  and  $\bar{t} = 0$  with  $\epsilon = 0.05$ ,  $k_{x,R} = 0.2$ ,  $l = 3$  and  $m_0 = 3$ .

578 Considering the richness of the phase space, further comparison between TWs and EPENS  
 579 for different parameters are warranted to fully understand their connection. One challenge in  
 580 searching for an TW is the daunting numerical process required to find a good initial guess,  
 581 whereas EPENS can be calculated much more rapidly using our approach. It is therefore  
 582 suggested that EPENS could be used as initial guesses in the search for TWs.

#### 3.4. Comparison with experimental data

584 Ricco & Alvarenga (2022) compared their linearised numerical results to the experimental  
 585 measurements by Wygnanski & Champagne (1973). For both the mean and perturbation flow,  
 586 excellent agreement was obtained at a low level of free-stream turbulence intensity, while  
 587 a significant deviation between the linear results and the experimental data was reported  
 588 for higher intensities. In figure 16, the experimental data at high turbulence intensity are  
 589 compared with our nonlinear results. The turbulence intensity was measured by  $(u_{rms}/\bar{U})_{cl}$   
 590 in Wygnanski & Champagne (1973), where the subscript  $cl$  refers to the value at the pipe axis.  
 591 The values of  $(u_{rms}/\bar{U})_{cl} = 5.8\%$  and  $7.8\%$  in Wygnanski & Champagne (1973) are found  
 592 to be equivalent to  $\epsilon = 0.082$  and  $0.12$  in our calculation for the case with  $k_{x,R} = 0.118$ ,  
 593  $l = 2$  and  $m_0 = 2$ . Figure 16(a) shows the good agreement in the mean-flow velocity  
 594 profiles except in the near-wall region where the numerical calculations underpredict the  
 595 experimental data. Good agreement also occurs in the comparison of the perturbation-flow  
 596 velocity profiles, as shown in figure 16(b). In Ricco & Alvarenga (2022), the velocity profile  
 597 was instead predicted by the linearised boundary-region equations to be zero at the pipe axis.  
 598 The finite perturbations near the pipe axis are well predicted when the nonlinear interactions  
 599 (i.e.  $r_l \hat{u}_{0,0}$ ) are taken into account. Both studies show the same trend: as the turbulent intensity  
 600 increases, a larger peak is reached, and the peak position moves towards the wall. The peak  
 601 of the profiles measured by Wygnanski & Champagne (1973) is obtained at a lower value and  
 602 located closer to the wall compared to our calculations. The disagreements are likely to come  
 603 from the different inflows at the pipe inlet. In experiments, the disturbances were generated  
 604 by an orifice plate or a circular disk placed at the inlet, and no precise information about  
 605 the resulting initial flow was given. The analytical expression (2.1) is instead used to model  
 606 the vortical disturbances in our calculations. As the flow is described by an initial-boundary

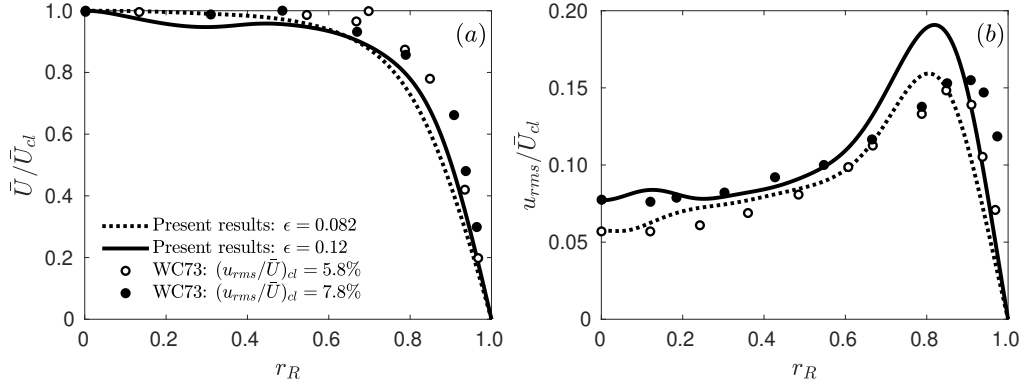


Figure 16: Comparison of (a) the mean flow and (b) the perturbation flow between the experimental measurements (circles) and present numerical results (lines) for  $Re_R = 1200$  at  $x_R = 30$ . Open and solid circles: experimental data measured by Wignanski & Champagne (1973) (refer to as WC73 in the figure) with  $(u_{rms}/\bar{U})_{cl} = 5.8\%$  and  $7.8\%$ . Dotted and solid lines: present results with  $\epsilon = 0.082, 0.12$ ,  $k_{x,R} = 0.118$ ,  $l = 2$  and  $m_0 = 2$ .

607 value problem in the pipe entrance, the inflow characteristics are crucial for an accurate  
608 prediction of the downstream development of the flow.

#### 609 4. Summary and conclusions

610 As a step towards understanding the laminar–turbulent transition in pipe flow, we have  
611 investigated the nonlinear evolution of free-stream vortical disturbances entrained in the  
612 entrance region of a circular pipe by using a high Reynolds number asymptotic approach. The  
613 oncoming disturbances are modelled by a pair of vortical modes with the same frequency but  
614 opposite azimuthal wavenumber. A long-wavelength hypothesis is utilised. This hypothesis is  
615 inspired by the experimental finding that streamwise-elongated streaks induced by free-stream  
616 disturbances in boundary layers amplify significantly (Matsubara & Alfredsson 2001). The  
617 disturbance amplitude is assumed to be intense enough for nonlinear interactions to occur.  
618 The present study can therefore be viewed as an extension of Ricco & Alvarenga (2022) to  
619 the nonlinear case.

620 The resultant nonlinear system is solved numerically by a marching procedure in the  
621 streamwise direction. A parametric study reveals the stabilising effect of nonlinearity on the  
622 intense algebraic disturbance growth near the pipe inlet. The linear theory thus overpredicts  
623 the nonlinear disturbance intensity. The effect of the Reynolds number, the streamwise and  
624 azimuthal wavelengths, and the radial length scale of the inlet disturbance on the nonlinear  
625 evolution of the disturbances is investigated. The mean-flow distortion  $\hat{u}_{0,0}$  grows significantly  
626 shortly downstream of the pipe inlet, being negative in the pipe core and positive near the  
627 wall, indicating an increase of wall-shear stress.

628 We report the formation, amplification and attenuation of rotationally symmetric elongated  
629 pipe-entrance nonlinear structures (EPENS). The distinct features of  $\mathcal{R}_h$ -EPENS ( $h > 1$ ) are  
630 equispaced  $h$  high-speed streaks around the pipe wall and  $h$  low-speed streaks in the pipe core.  
631 A remarkable resemblance between these structures and nonlinear travelling waves (TWs)  
632 occurring in fully developed pipe flow is noted for  $m_0 = 3, 5, 6$ . Rotationally asymmetric  
633 EPENS are discovered for  $m_0 = 1$ . They also agree well with asymmetric TWs for  $m_0 = 1$ .  
634 These similarities may shed light on the physical origin of nonlinear TWs. The robustness  
635 of the EPENS in response to changes of different inlet flow conditions is demonstrated,



636 indicating that the EPENS are likely to be a strong attractor of the dynamical system. We  
 637 also suggest the potential use of EPENS as an initial guess in the numerical search for the  
 638 nonlinear TWs. More investigations are necessary to clarify the connection between the  
 639 EPENS and the TWs.

640 With the inclusion of nonlinear effects, good agreement between our calculations and  
 641 the experimental measurements of Wygnanski & Champagne (1973) is obtained for both  
 642 the mean flow and the perturbation flow. Further improvement may be gained by using  
 643 a continuous spectrum of free-stream disturbances as oncoming disturbances. Performing  
 644 a secondary instability analysis of the EPENS is also of interest. The EPENS attenuate  
 645 downstream in our calculation, but they may persist when the growth of small-amplitude  
 646 secondary disturbances is taken into account.

647 It is our hope that the theoretical work presented herein will motivate more direct numerical  
 648 simulations and experimental investigations in the entrance region of pipe flow.

649 **Acknowledgements.** The authors would like to thank the Faculty of Engineering of the University of  
 650 Sheffield for funding this research. The authors are also indebted to Dr Elena Marensi for her insightful  
 651 comments.

652 **Funding.** This work was funded by Faculty of Engineering University Research Scholarship from University  
 653 of Sheffield.

654 **Declaration of interests.** The authors report no conflict of interest.

## 655 Appendix A. Conservation of the mass flow rate

656 At each instant in time and at each streamwise location, the mass flow rate is conserved.  
 657 Since the flow is incompressible, this condition translates to the conservation of the bulk  
 658 velocity, i.e. the streamwise velocity averaged on the cross-section of the pipe is equal to the  
 659 oncoming velocity  $U_\infty^*$ :

$$660 \quad \frac{1}{\pi R^2} \int_0^{2\pi} \int_0^R (U + r_t \bar{u}) r dr d\theta = 1. \quad (\text{A } 1)$$

661 Substituting (2.7) into (A 1), equation (2.11) is obtained for the laminar base flow and

$$662 \quad \sum_{m,n=-\infty}^{\infty} \int_0^{2\pi} \int_0^R \hat{u}_{m,n} e^{im\theta + in\bar{t}} r dr d\theta = 0. \quad (\text{A } 2)$$

663 By using the orthogonality property of the Fourier series, equation (2.20) is obtained, which is  
 664 the condition needed to solve the system because the pressure  $\Gamma_{0,n}$  is an additional unknown.

## 665 Appendix B. Coefficients of equation (2.27)

The expressions of  $\{\widehat{V}, \widehat{V}_r, \widehat{V}_x, \dots, \widehat{U}_{xrr}\}$  in equation (2.27) are

$$\begin{aligned} \widehat{V} &= \left(1 - \frac{1}{m^2}\right) \left(in + \frac{\partial V}{\partial r} + \frac{m^2 - 1}{\mathcal{F} r^2}\right) + \frac{2r}{m^2} \frac{\partial^2 U}{\partial \bar{x} \partial r} + \frac{r^2}{m^2} \frac{\partial^3 U}{\partial \bar{x} \partial r^2}, \\ \widehat{V}_r &= \left[ \left(1 - \frac{4}{m^2}\right) V - \frac{3r}{m^2} \left(in + \frac{\partial V}{\partial r}\right) - \left(2 + \frac{1}{m^2}\right) \frac{1}{\mathcal{F} r} \right] + \frac{r^2}{m^2} \frac{\partial^2 U}{\partial \bar{x} \partial r}, \\ \widehat{V}_x &= \left(1 - \frac{1}{m^2}\right) U + \frac{r}{m^2} \left(\frac{\partial U}{\partial r} + r \frac{\partial^2 U}{\partial r^2}\right), \end{aligned}$$

$$\begin{aligned}
\widehat{V}_{rr} &= - \left[ \frac{r}{m^2} \left( inr + 5V + r \frac{\partial V}{\partial r} \right) + \left( 2 - \frac{5}{m^2} \right) \frac{1}{\mathcal{F}} \right], \\
\widehat{V}_{xr} &= - \frac{3Ur}{m^2}, \\
\widehat{V}_{rrr} &= - \frac{r}{m^2} \left( rV - \frac{6}{\mathcal{F}} \right), \\
\widehat{V}_{xrr} &= - \frac{r^2 U}{m^2}, \\
\widehat{V}_{rrrr} &= \frac{r^2}{m^2 \mathcal{F}}, \\
\widehat{U} &= \frac{\partial V}{\partial \bar{x}} + \frac{2r}{m^2} \frac{\partial^2 U}{\partial \bar{x}^2} + \frac{r^2}{m^2} \frac{\partial^3 U}{\partial \bar{x}^2 \partial r}, \\
\widehat{U}_r &= \frac{r}{m^2} \frac{\partial V}{\partial \bar{x}}, \\
\widehat{U}_x &= - \frac{2}{\mathcal{F}r} + \frac{6r}{m^2} \frac{\partial U}{\partial \bar{x}} + \frac{2r^2}{m^2} \frac{\partial^2 U}{\partial \bar{x} \partial r}, \\
\widehat{U}_{rr} &= \frac{r^2}{m^2} \frac{\partial V}{\partial \bar{x}}, \\
\widehat{U}_{xr} &= \frac{2}{m^2} \left( \frac{1}{\mathcal{F}} - 2Vr - r^2 \frac{\partial V}{\partial r} \right), \\
\widehat{U}_{xrr} &= \frac{2r}{m^2 \mathcal{F}}.
\end{aligned}$$

### 666 Appendix C. Modified block tridiagonal matrix algorithm

667 A modified block tridiagonal matrix algorithm is devised for solving the discretised version  
668 of system (2.30)-(2.32) together with the discretised (2.20) for  $m = 0$ ,

$$669 \quad \mathbf{A}\boldsymbol{\delta} = \mathbf{b}. \quad (\text{C1})$$

670 In expanded form, the system (C1) is

$$671 \quad \begin{bmatrix} A_1 & C_1 & & & & & & E_1 \\ B_2 & A_2 & C_2 & & & & & E_2 \\ & \dots & \dots & \dots & & & & \dots \\ & & & B_j & A_j & C_j & & E_j \\ & & & & \dots & \dots & \dots & \dots \\ & & & & & B_{J-3} & A_{J-3} & C_{J-3} & E_{J-3} \\ & & & & & B_{J-2} & A_{J-2} & E_{J-2} & \delta_{J-2} \\ D_1 & D_2 & D_3 & \dots & & D_{J-2} & 0 & \Pi & 0 \end{bmatrix} \begin{bmatrix} \delta_1 \\ \delta_2 \\ \dots \\ \delta_j \\ \dots \\ \delta_{J-3} \\ \delta_{J-2} \\ \Pi \end{bmatrix} = \begin{bmatrix} b_1 \\ b_2 \\ \dots \\ b_j \\ \dots \\ b_{J-3} \\ b_{J-2} \\ 0 \end{bmatrix} \quad (\text{C2})$$

672 where  $A_j$ ,  $B_j$  and  $C_j$  are  $3 \times 3$  matrices,  $E_j$ ,  $\delta_j$  and  $b_j$  are  $3 \times 1$  matrices,  $D_j$  is a  $1 \times 3$   
673 matrix, and  $\Pi$  is a scalar. In equation (C2), row  $j$  for  $2 \leq j \leq J-3$  represents the discretised  
674 equations (2.30)–(2.32) at the interior nodes, while rows 1 and  $J-2$  refer to the equations at  
675 the boundaries. The last row is the discretised integral (2.20).

676 First, we add any two decoupled equations to the system in order to add two rows at the  
677 bottom of matrix  $\mathbf{A}$  and two columns on the right of matrix  $\mathbf{A}$ . This step makes  $D_j$  and  $E_j$   
678  $3 \times 3$  matrices, and creates two  $3 \times 1$  matrices,  $\delta_{J-1}$  and  $b_{J-1}$ , at the bottom of  $\boldsymbol{\delta}$  and  $\mathbf{b}$ , which  
679 is necessary in order to render the system suitable for the block elimination. The matrices

680  $D_j$  and  $E_j$  are renamed  $\mathcal{D}_j$  and  $\mathcal{E}_j$ . The system (C2) becomes

$$681 \begin{bmatrix} A_1 & C_1 & & & & & & \mathcal{E}_1 \\ B_2 & A_2 & C_2 & & & & & \mathcal{E}_2 \\ & \dots & \dots & \dots & & & & \dots \\ & & B_j & A_j & C_j & & & \mathcal{E}_j \\ & & & \dots & \dots & \dots & & \dots \\ & & & & B_{J-3} & A_{J-3} & C_{J-3} & \mathcal{E}_{J-3} \\ & & & & B_{J-2} & A_{J-2} & \mathcal{E}_{J-2} & \mathcal{E}_{J-2} \\ \mathcal{D}_1 & \mathcal{D}_2 & \mathcal{D}_3 & \dots & & \mathcal{D}_{J-2} & \mathcal{E}_{J-1} & \mathcal{E}_{J-1} \end{bmatrix} \begin{bmatrix} \delta_1 \\ \delta_2 \\ \dots \\ \delta_j \\ \dots \\ \delta_{J-3} \\ \delta_{J-2} \\ \delta_{J-1} \end{bmatrix} = \begin{bmatrix} b_1 \\ b_2 \\ \dots \\ b_j \\ \dots \\ b_{J-3} \\ b_{J-2} \\ b_{J-1} \end{bmatrix} \quad (\text{C3})$$

682 The standard block tridiagonal matrix algorithm described in Cebeci (2002) is modified to  
683 solve (C3), which also consists of the forward sweep and backward substitution. However,  
684 in each forward sweep, one more step needs to be performed to eliminate  $\mathcal{D}_j$ , which leads to

$$685 \begin{bmatrix} I & C'_1 & & & & & & \mathcal{E}'_1 \\ & I & C'_2 & & & & & \mathcal{E}'_2 \\ & & \dots & \dots & & & & \dots \\ & & & I & C'_j & & & \mathcal{E}'_j \\ & & & & \dots & \dots & & \dots \\ & & & & & I & C'_{J-3} & \mathcal{E}'_{J-3} \\ & & & & & I & \mathcal{E}'_{J-2} & \mathcal{E}'_{J-2} \\ & & & & & & \mathcal{E}'_{J-1} & \mathcal{E}'_{J-1} \end{bmatrix} \begin{bmatrix} \delta_1 \\ \delta_2 \\ \dots \\ \delta_j \\ \dots \\ \delta_{J-3} \\ \delta_{J-2} \\ \delta_{J-1} \end{bmatrix} = \begin{bmatrix} b'_1 \\ b'_2 \\ \dots \\ b'_j \\ \dots \\ b'_{J-3} \\ b'_{J-2} \\ b'_{J-1} \end{bmatrix} \quad (\text{C4})$$

686 where the prime denotes the new coefficients. The solution is then obtained by backward  
687 substitution:

$$688 \begin{cases} \delta_{J-1} = \mathcal{E}'_{J-1}^{-1} b'_{J-1}, \\ \delta_{J-2} = b'_{J-2} - \mathcal{E}'_{J-2} \delta_{J-1} \\ \delta_i = b'_i - C'_i \delta_{i+1} - \mathcal{E}'_i \delta_{J-1}, \quad i = J-3, J-4, \dots, 1. \end{cases} \quad (\text{C5})$$

## REFERENCES

- 689 AVILA, M., BARKLEY, D. & HOF, B. 2023 Transition to turbulence in pipe flow. *Annu. Rev. Fluid Mech.* **55**,  
690 575–602.
- 691 BATCHELOR, G.K. & GILL, A.E. 1962 Analysis of the stability of axisymmetric jets. *J. Fluid Mech.* **14**,  
692 529–551.
- 693 BERGSTRÖM, L. 1992 Initial algebraic growth of small angular dependent disturbances in pipe Poiseuille  
694 flow. *Stud. Appl. Maths.* **87** (1), 61–79.
- 695 BERGSTRÖM, L. 1993 Optimal growth of small disturbances in pipe Poiseuille flow. *Phys. Fluids A* **5** (11),  
696 2710–2720.
- 697 BORODULIN, V. I., IVANOV, A. V., KACHANOV, Y. S. & ROSCHEKTAYEV, A. P. 2021 Distributed vortex  
698 receptivity of a swept-wing boundary layer. Part 1. Efficient excitation of cf modes. *J. Fluid Mech.*  
699 **908**, A14.
- 700 BÖBERG, L. & BRÖSA, U. 1988 Onset of turbulence in a pipe. *Z. Naturforsch. A* **43** (8-9), 697–726.
- 701 CEBECI, T. 2002 *Convective heat transfer*. Springer.
- 702 CHRISTIANSEN, E.B. & LEMMON, H.E. 1965 Entrance region flow. *AIChE J.* **11** (6), 995–999.
- 703 CORCOS, G.M. & SELLARS, J.R. 1959 On the stability of fully developed flow in a pipe. *J. Fluid Mech.* **5** (1),  
704 97–112.
- 705 CROWDER, H.J. & DALTON, C. 1971 On the stability of Poiseuille flow in a pipe. *J. Comp. Phys.* **7** (1), 12–31.
- 706 DAVEY, A. 1978 On Itoh's finite amplitude stability theory for pipe flow. *J. Fluid Mech.* **86** (4), 695–703.
- 707 DAVEY, A. & DRAZIN, P.G. 1969 The stability of Poiseuille flow in a pipe. *J. Fluid Mech.* **36** (2), 209–218.
- 708 DAVEY, A. & NGUYEN, H.P.F. 1971 Finite-amplitude stability of pipe flow. *J. Fluid Mech.* **45** (4), 701–720.

- 709 DIETZ, A. J. 1999 Local boundary-layer receptivity to a convected free-stream disturbance. *J. Fluid Mech.*  
710 **378**, 291–317.
- 711 ECKHARDT, B., SCHNEIDER, T.M., HOF, B. & WESTERWEEL, J. 2007 Turbulence transition in pipe flow. *Annu.*  
712 *Rev. Fluid Mech.* **39** (1), 447–468.
- 713 FAISST, H. & ECKHARDT, B. 2003 Traveling waves in pipe flow. *Phys. Rev. Lett.* **91** (22), 224502.
- 714 GARG, V.K. 1981 Stability of developing flow in a pipe: non-axisymmetric disturbances. *J. Fluid Mech.* **110**,  
715 209–216.
- 716 GARG, V.K. 1983 Stability of nonparallel developing flow in a pipe to nonaxisymmetric disturbances. *J.*  
717 *Appl. Mech.* **50** (1), 210.
- 718 GARG, V.K. & GUPTA, S.C. 1981 Stability of developing flow in a pipe-nonparallel effects. *J. Appl. Mech.*  
719 **48** (2), 243.
- 720 GARG, V.K. & ROULEAU, W.T. 1972 Linear spatial stability of pipe Poiseuille flow. *J. Fluid Mech.* **54** (1),  
721 113–127.
- 722 GILL, A.E. 1965 On the behaviour of small disturbances to Poiseuille flow in a circular pipe. *J. Fluid Mech.*  
723 **21** (1), 145–172.
- 724 GRAHAM, M. D. & FLORYAN, D. 2021 Exact coherent states and the nonlinear dynamics of wall-bounded  
725 turbulent flows. *Annu. Rev. Fluid Mech.* **53** (Volume 53, 2021), 227–253.
- 726 GUPTA, S.C. & GARG, V.K. 1981 Effect of velocity distribution on the stability of developing flow in a pipe.  
727 *Phys. Fluids* **24** (4), 576–578.
- 728 HAGEN, G. 1839 Ueber die bewegung des wassers in engen cylindrischen röhren. *Annalen der Physik* **122** (3),  
729 423–442.
- 730 HOF, B., VAN DOORNE, C.W.H., WESTERWEEL, J. & NIEUWSTADT, F.T.M. 2005 Turbulence regeneration in  
731 pipe flow at moderate Reynolds numbers. *Phys. Rev. Lett.* **95** (21), 214502.
- 732 HOF, B., VAN DOORNE, C.W.H., WESTERWEEL, J., NIEUWSTADT, F.T.M., FAISST, H., ECKHARDT, B., WEDIN,  
733 H., KERSWELL, R.R. & WALEFFE, F. 2004 Experimental observation of nonlinear traveling waves in  
734 turbulent pipe flow. *Science* **305** (5690), 1594–1598.
- 735 HORNBECK, R.W. 1964 Laminar flow in the entrance region of a pipe. *Appl. Sci. Res.* **13**, 224–232.
- 736 HUANG, L.M. & CHEN, T.S. 1974a Stability of the developing laminar pipe flow. *Phys. Fluids* **17** (1),  
737 245–247.
- 738 HUANG, L.M. & CHEN, T.S. 1974b Stability of developing pipe flow subjected to non-axisymmetric  
739 disturbances. *J. Fluid Mech.* **63** (1), 183–193.
- 740 ITOH, N. 1977 Nonlinear stability of parallel flows with subcritical Reynolds numbers. Part 2. Stability of  
741 pipe Poiseuille flow to finite axisymmetric disturbances. *J. Fluid Mech.* **82** (3), 469–479.
- 742 KERSWELL, R.R. 2005 Recent progress in understanding the transition to turbulence in a pipe. *Nonlinearity*  
743 **18** (6), R17.
- 744 KERSWELL, R.R. 2018 Nonlinear nonmodal stability theory. *Annu. Rev. Fluid Mech.* **50** (1), 319–345.
- 745 KERSWELL, R.R., PRINGLE, C.C.T. & WILLIS, A.P. 2014 An optimization approach for analysing nonlinear  
746 stability with transition to turbulence in fluids as an exemplar. *Rep. Prog. Phys.* **77** (8), 085901.
- 747 KERSWELL, R.R. & TUTTY, O.R. 2007 Recurrence of travelling waves in transitional pipe flow. *J. Fluid Mech.*  
748 **584**, 69–102.
- 749 KHORRAMI, M.R., MALIK, M.R. & ASH, R.L. 1989 Application of spectral collocation techniques to the  
750 stability of swirling flows. *J. Comp. Phys.* **81** (1), 206–229.
- 751 LANGHAAR, H.L. 1942 Steady flow in the transition length of a straight tube. *J. Appl. Mech.* **9** (2), A55–A58.
- 752 LEIB, S.J., WUNDROW, D.W. & GOLDSTEIN, M.E. 1999 Effect of free-stream turbulence and other vortical  
753 disturbances on a laminar boundary layer. *J. Fluid Mech.* **380**, 169–203.
- 754 LEWIS, H.R. & BELLAN, P.M. 1990 Physical constraints on the coefficients of fourier expansions in cylindrical  
755 coordinates. *J. Math. Phys.* **31** (11), 2592–2596.
- 756 MARENSI, E. & RICCO, P. 2017 Growth and wall-transpiration control of nonlinear unsteady Görtler vortices  
757 forced by free-stream vortical disturbances. *Phys. Fluids* **29** (11), 114106.
- 758 MARENSI, E., RICCO, P. & WU, X. 2017 Nonlinear unsteady streaks engendered by the interaction of  
759 free-stream vorticity with a compressible boundary layer. *J. Fluid Mech.* **817**, 80–121.
- 760 MATSUBARA, M. & ALFREDSSON, P.H. 2001 Disturbance growth in boundary layers subjected to free-stream  
761 turbulence. *J. Fluid Mech.* **430**, 149–168.
- 762 MESEGUER, A. & TREFETHEN, L.N. 2003 Linearized pipe flow to Reynolds number 107. *J. Comp. Phys.*  
763 **186** (1), 178–197.

- 764 O'SULLIVAN, P.L. & BREUER, K.S. 1994 Transient growth in circular pipe flow. I. Linear disturbances. *Phys. Fluids* **6** (11), 3643–3651.
- 765
- 766 PATERA, A.T. & ORSZAG, S.A. 1981 Finite-amplitude stability of axisymmetric pipe flow. *J. Fluid Mech.* **112**, 467–474.
- 767
- 768 PEKERIS, C.L. 1948 Stability of the laminar flow through a straight pipe of circular cross-section to infinitesimal disturbances which are symmetrical about the axis of the pipe. *Proc. Natl Acad. Sci.* **34** (6), 285–295.
- 769
- 770
- 771 PFENNIGER, W 1961 Transition in the inlet length of tubes at high Reynolds numbers. *Boundary layer and flow control* pp. 970–980.
- 772
- 773 POISEUILLE, J.L. 1844 *Recherches expérimentales sur le mouvement des liquides dans les tubes de très-petits diamètres*. Imprimerie Royale.
- 774
- 775 POPE, S.B. 2000 *Turbulent flows*. Cambridge University Press.
- 776 PRINGLE, C.C.T., DUGUET, Y. & KERSWELL, R.R. 2009 Highly symmetric travelling waves in pipe flow. *Phil. Trans. R. Soc. A* **367** (1888), 457–472.
- 777
- 778 PRINGLE, C.C.T. & KERSWELL, R.R. 2007 Asymmetric, helical, and mirror-symmetric traveling waves in pipe flow. *Phys. Rev. Lett.* **99** (7), 074502.
- 779
- 780 PRINGLE, C.C.T. & KERSWELL, R.R. 2010 Using nonlinear transient growth to construct the minimal seed for shear flow turbulence. *Phys. Rev. Lett.* **105**, 154502.
- 781
- 782 PRINGLE, C.C.T., WILLIS, A.P. & KERSWELL, R.R. 2012 Minimal seeds for shear flow turbulence: using nonlinear transient growth to touch the edge of chaos. *J. Fluid Mech.* **702**, 415–443.
- 783
- 784 RAYLEIGH, L. 1892 On the question of the stability of the flow of fluids. *Philos. Mag.* **34** (206), 59–70.
- 785 RESHOTKO, E. & TUMIN, A. 2001 Spatial theory of optimal disturbances in a circular pipe flow. *Phys. Fluids* **13** (4), 991–996.
- 786
- 787 REYNOLDS, O. 1883 XXIX. An experimental investigation of the circumstances which determine whether the motion of water shall be direct or sinuous, and of the law of resistance in parallel channels. *Phil. Trans. R. Soc.* (174), 935–982.
- 788
- 789
- 790 RICCO, P. & ALVARENGA, C. 2021 Entrainment and growth of vortical disturbances in the channel-entrance region. *J. Fluid Mech.* **927**, A18.
- 791
- 792 RICCO, P. & ALVARENGA, C. 2022 Growth of vortical disturbances entrained in the entrance region of a circular pipe. *J. Fluid Mech.* **932**, A16.
- 793
- 794 RICCO, P., LUO, J. & WU, X. 2011 Evolution and instability of unsteady nonlinear streaks generated by free-stream vortical disturbances. *J. Fluid Mech.* **677**, 1–38.
- 795
- 796 SALWEN, H. & GROSCH, C.E. 1972 The stability of Poiseuille flow in a pipe of circular cross-section. *J. Fluid Mech.* **54** (1), 93–112.
- 797
- 798 SARPKAYA, T. 1975 A note on the stability of developing laminar pipe flow subjected to axisymmetric and non-axisymmetric disturbances. *J. Fluid Mech.* **68** (2), 345–351.
- 799
- 800 SCHMID, P.J. 2007 Nonmodal stability theory. *Annu. Rev. Fluid Mech.* **39** (1), 129–162.
- 801 SCHMID, P.J. & HENNINGSON, D.S. 1994 Optimal energy density growth in Hagen–Poiseuille flow. *J. Fluid Mech.* **277**, 197–225.
- 802
- 803 SEXL, T. 1927 Zur stabilitätsfrage der Poiseuilleschen und Couetteschen strömung. *Ann. Phys.* **388** (14), 835–848.
- 804
- 805 SHEN, F.C.T., CHEN, T.S. & HUANG, L.M. 1976 The effects of main-flow radial velocity on the stability of developing laminar pipe flow. *J. Appl. Mech.* **43** (2), 209.
- 806
- 807 DA SILVA, D.F. & MOSS, E.A. 1994 The stability of pipe entrance flows subjected to axisymmetric disturbances. *J. Fluids Engng* **116** (1), 61–65.
- 808
- 809 SMITH, F.T. & BODONYI, R.J. 1982 Amplitude-dependent neutral modes in the Hagen–Poiseuille flow through a circular pipe. *Proc. R. Soc. Lond. A* **384** (1787), 463–489.
- 810
- 811 SPARROW, E.M., LIN, S.H. & LUNDGREN, T.S. 1964 Flow development in the hydrodynamic entrance region of tubes and ducts. *Phys. Fluids* **7** (3), 338–347.
- 812
- 813 TATSUMI, T. 1952 Stability of the laminar inlet-flow prior to the formation of Poiseuille regime, II. *J. Phys. Soc. Japan* **7** (5), 495–502.
- 814
- 815 TUCKERMAN, L.S. 1989 Divergence-free velocity fields in nonperiodic geometries. *J. Comp. Phys.* **80** (2), 403–441.
- 816
- 817 TUMIN, A. 1996 Receptivity of pipe Poiseuille flow. *J. Fluid Mech.* **315**, 119–137.
- 818 WALEFFE, F. 1997 On a self-sustaining process in shear flows. *Phys. Fluids* **9** (4), 883–900.

- 819 WEDIN, H. & KERSWELL, R.R. 2004 Exact coherent structures in pipe flow: travelling wave solutions. *J.*  
820 *Fluid Mech.* **508**, 333–371.
- 821 WILLIS, A. P., DUGUET, Y., OMEL'CHENKO, O. & WOLFRUM, M. 2017 Surfing the edge: using feedback  
822 control to find nonlinear solutions. *J. Fluid Mech.* **831**, 579–591.
- 823 WILLIS, A. P. & KERSWELL, R. R. 2008 Coherent structures in localized and global pipe turbulence. *Phys.*  
824 *Rev. Lett.* **100** (12), 124501.
- 825 WU, X., MOIN, P. & ADRIAN, R.J. 2020 Laminar to fully turbulent flow in a pipe: scalar patches, structural  
826 duality of turbulent spots and transitional overshoot. *J. Fluid Mech.* **896**, A9.
- 827 WU, X., MOIN, P., ADRIAN, R.J. & BALTZER, J.R. 2015 Osborne Reynolds pipe flow: Direct simulation from  
828 laminar through gradual transition to fully developed turbulence. *Proc. Natl Acad. Sci.* **112** (26),  
829 7920–7924.
- 830 WYGNANSKI, I.J. & CHAMPAGNE, F.H. 1973 On transition in a pipe. Part 1. The origin of puffs and slugs and  
831 the flow in a turbulent slug. *J. Fluid Mech.* **59** (2), 281–335.
- 832 WYGNANSKI, I., SOKOLOV, M. & FRIEDMAN, D. 1975 On transition in a pipe. Part 2. The equilibrium puff.  
833 *J. Fluid Mech.* **69** (2), 283–304.
- 834 ZANOUN, E.-S., KITO, M. & EGBERS, C. 2009 A study on flow transition and development in circular and  
835 rectangular ducts. *J. Fluids Engng* **131** (6), 061204.